

Article

# Columbite U-Pb Geochronology of Kalu'an Lithium Pegmatites in Northern Xinjiang, China: Implications for Genesis and Emplacement History of Rare-Element Pegmatites

Yonggang Feng <sup>1,2,3,\*</sup> , Ting Liang <sup>1,2,\*</sup>, Ze Zhang <sup>1,2</sup>, Yiqian Wang <sup>1,2</sup>, Yi Zhou <sup>1</sup>, Xiuqing Yang <sup>1,2</sup>, Jinggang Gao <sup>1</sup>, Hui Wang <sup>1</sup> and Kun Ding <sup>1</sup>

<sup>1</sup> School of Earth Science and Resources, Chang'an University, Xi'an 710054, China

<sup>2</sup> Laboratory of Mineralization and Dynamics, Chang'an University, Xi'an 710054, China

<sup>3</sup> Department of Earth Sciences, Western University, London, Ontario N6A 3K7, Canada

\* Correspondence: ygfeng@chd.edu.cn (Y.F.); liangt@chd.edu.cn (T.L.)

Received: 20 May 2019; Accepted: 23 July 2019; Published: 25 July 2019



**Abstract:** The Kalu'an-Azubai pegmatite field, one of the most important rare-metal metallogenic regions in China, contains a large number of pegmatite dikes belonging to spodumene and lepidolite subtypes. Columbite-group minerals (CGMs) collected from three spodumene subtype pegmatites (No. 802, No. 803, and No. 805 pegmatites) were analyzed for major element contents using EPMA (electron probe micro-analyzer) and dated using LA-ICP-MS (laser ablation-inductively coupled plasma mass spectrometer). The crystallization ages of the CGMs from No. 802, No. 803, and No. 805 pegmatites are  $209.5 \pm 1.4$  Ma ( $2\sigma$ ),  $198.3 \pm 2.0$  Ma ( $2\sigma$ ), and  $224.3 \pm 2.9$  Ma ( $2\sigma$ ), respectively. Oscillatory zoning and/or sector zoning along with the associated mineral assemblages suggest that the dated columbite is of magmatic origin. The crystallization ages of the columbite grains thus represent the emplacement ages of the Li pegmatites. Therefore, our dating results indicate that there were three emplacement events of the Li-rich pegmatite-forming melts in a timeframe of ~30 Ma. In combination with previous studies, we conclude that the Li pegmatites were formed before the Be-Ta-Nb pegmatites (~194–192 Ma), which precludes the genesis of rare-metal pegmatites via fractional crystallization of a granitic magma in the Kalu'an-Azubai region.

**Keywords:** columbite; U-Pb dating; Li pegmatite; Kalu'an; Chinese Altay orogen

## 1. Introduction

The Kalu'an-Azubai pegmatite field, located in the Chinese Altay orogen, is one of the most important pegmatite fields for rare element (Li, Be, Nb, and Ta) resources and gemstone (mainly aquamarine) exploration in China [1–5]. Recently, this pegmatite field has attracted increasing attention not only because of the high global demand for lithium but also because of the pegmatite-granite relationship that has long puzzled geologists [2]. The well-defined regional zonation of the pegmatite group including barren pegmatites, Be-Ta-Nb pegmatites, and Li pegmatites, likely suggests that the exotic pegmatites formed through fractional crystallization of a granitic magma [2]. Yet recently reported chronological data precluded a direct genetic link between the rare-element pegmatites and their nearby granitic pluton (the Halong granite) [3–5]. According to these studies [3–5], the Halong granite was emplaced at 403.3–400.9 Ma whereas the emplacement ages of the rare-element pegmatites vary from  $227.9 \pm 2.6$  Ma to  $191.6 \pm 2.0$  Ma. Nevertheless, interpretation of the Zircon U-Pb ages reported for the rare-element pegmatites in the region remains ambiguous due to: (1) the presence of xenocrystic zircon, (2) discordancy caused by Pb-loss from high-U zircon, (3) the presence of recrystallized zircons

and/or late-stage hydrothermal zircons [3,4]. Therefore, the emplacement ages of the rare-element pegmatites in the Kalu'an-Azubai region need to be precisely determined to reconstruct the timeframe of pegmatite emplacement and explore the petrogenesis of the rare-element pegmatites.

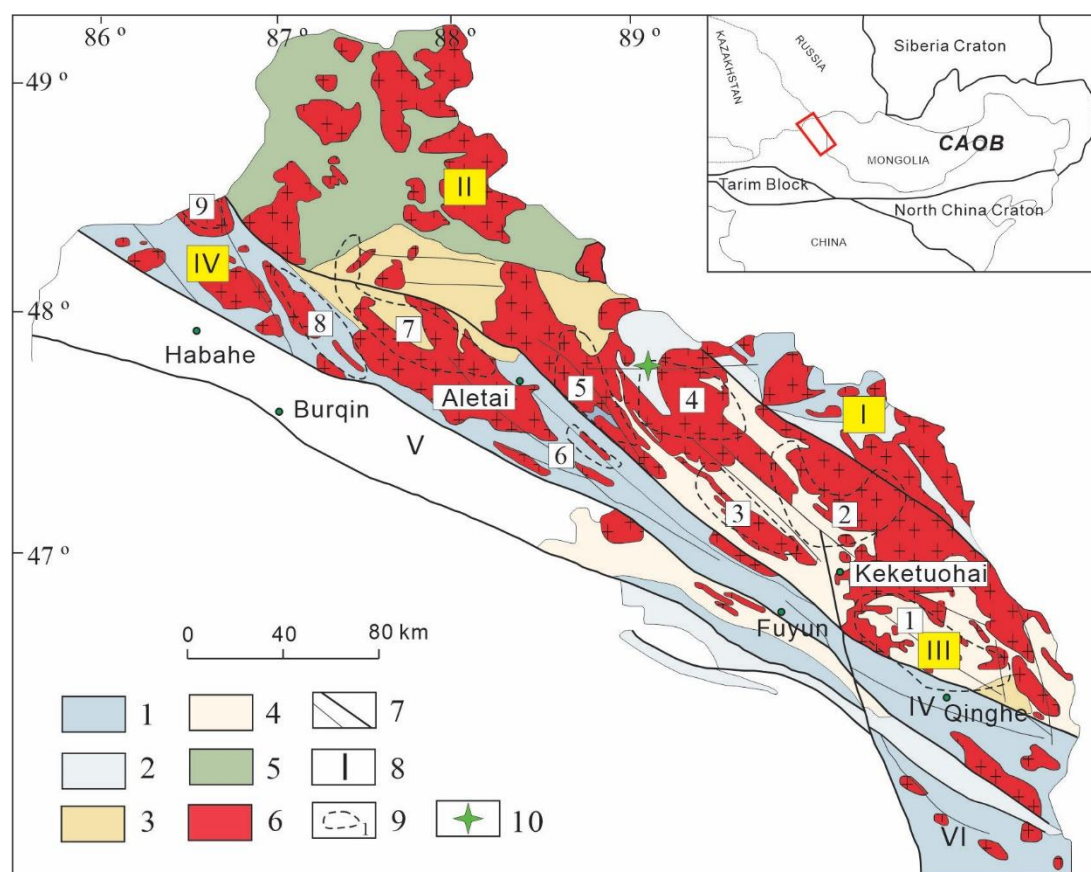
Columbite-tantalite group minerals (CGMs) are an important source for strategic elements, Nb and Ta, in highly evolved granites and granitic pegmatites [6,7]. These minerals share a general chemical formula  $AB_2O_6$ , in which A is occupied by divalent cations including  $Fe^{2+}$ ,  $Mn^{2+}$ , and rarely  $Mg^{2+}$  and B, by  $Nb^{5+}$  and  $Ta^{5+}$  [8–11]. Columbite-group minerals are suitable for dating granitic rocks [10,12–14], and columbite U-Pb dating, in particular, has proved to be useful for determining emplacement or mineralization ages of granitic pegmatites [13–24] because U is sufficiently high and the compatibility of Pb is low in the CGM lattice. Recent studies also showed that CGMs are more resistant to hydrothermal alteration than zircons from the same pegmatites [21]. Moreover, CGMs mainly crystallize from pegmatite-forming melts or during metasomatism at magmatic stages (cf. [25]) and inherited CGMs do not occur in granitic rocks [12]. Therefore, columbite U-Pb dating can provide reliable ages for highly evolved pegmatites by avoiding the above-mentioned issues affecting zircon. Compared with ID-TIMS U-Pb dating, in situ dating techniques such as LA-ICP-MS (laser ablation-inductively coupled plasma mass spectrometer) and SIMS (secondary ion mass spectrometer) can avoid uranium-rich inclusions (e.g., uraninite) that are commonly present in CGMs and tedious sample preparation [14]. Thus, in situ dating techniques have been increasingly applied to columbite U-Pb dating [14,21–23].

In this contribution, we dated three representative Li pegmatite dikes (No. 802, No. 803, and No. 805 pegmatites) in the Kalu'an-Azubai pegmatite field using the columbite LA-ICP-MS dating method. The obtained columbite U-Pb ages were then compared with the zircon U-Pb ages in previous studies and used to reconstruct the timeframe of the pegmatite field. In light of the new age data, the petrogenesis of the rare-element pegmatites was also explored.

## 2. Geological Setting

The Chinese Altay orogen is located in the northern part of Xinjiang Uygur Autonomous Region, China and extends eastwards to Mongolia and westwards to Kazakhstan and Russia ([26–33], Figure 1). This orogen is regarded as one of the most important rare-metal metallogenic belts in China [2,5,34,35]. Windley et al. [26] divided the Chinese Altay orogen into six fault-bounded terranes, including the Altaishan terrane, the Northwest Altaishan terrane, the Central Altaishan terrane, the Qiongkuer–Abagong terrane, the Erqis terrane, and the Burkin–Ertai terrane (Figure 1). The Altaishan terrane is dominated by Late Devonian to Early Carboniferous metasedimentary rocks overlain by shale, siltstone, greywackes, and limestone [26,34]. The Northwest Altaishan terrane is mainly composed of Neoproterozoic–Early Devonian metasediments and schists that are unconformably overlain by shale, limestone, and andesitic breccia [5,34]. The Central Altaishan terrane is dominated by Neoproterozoic–Silurian amphibolite-facies gneisses, greenschist-facies metasediments, and metavolcanics [5]. The Qiongkuer–Abagong terrane mainly consists of Upper Silurian–Lower Devonian arc andesitic volcanic and volcanic clastic rocks with lesser basaltic rocks [28,34]. These rocks are overlain by Middle Devonian turbiditic sandstone-shale-succession associated with basaltic pillow lavas [26,34]. The southeastern part of the Erqis terrane consists of a Precambrian basement (dominated by high-grade gneiss and schist) and Late Carboniferous sedimentary rocks whereas the northwestern part is largely covered by Quaternary sediments [26,34]. The Perkin–Ertai terrane consists of Devonian to Carboniferous metamorphosed sedimentary and volcanic rocks [26]. All the terranes are dominated by Paleozoic granitoids [5,26].

Nine metallogenic districts with various rare-metal mineralization in the Central Altaishan and Qiongkuer–Abagong terranes (Figure 1) have been recognized by Zou & Li [2]. According to [2,5], the Qinghe and Dakalasu–Kekexier districts are mainly characterized by Be-Nb-Ta mineralization whereas the Xiaokalasu–Qiebielin and Kelumute–Jideke districts host Li-Be-Nb-Ta mineralization. The Keketuohai district is famous for complex Li-Be-Nb-Ta-(Rb-Cs) mineralization [2].



1- Late Carboniferous metasediment-metavolcanics; 2-Devonian pyroclastic rocks; 3-Silurian gneisses; 4-Ordovician Schists and gneisses; 5-Neoproterozoic–Early Devonian metasediments and schists; 6-Paleozoic granitoids; 7-faults; 8-tectonic terranes; 9-metallogenic districts; 10-study area

Tectonic terranes:

I-Altaihan; II-Northwest Altaishan; III-Central Altaishan; IV-Qiongkuer-Abagong; V-Erqis; VI-Burqin-Ertai

Metallogenic districts:

1-Qinghe; 2-Keketuohai; 3-Kuwei-Jiebierte; 4-Kelumute-Jideke; 5-Kala'e'erqisi; 6-Dakalasu-Kekexi'er; 7-Xiaokalasu-Qiebielin; 8-Hailutan-Yeliuman; 9-Jiamanhaba

**Figure 1.** Geological map of the Chinese Altay orogen (after [2,3]). Abbreviations: CAOB = the Central Asian Orogenic Belt.

### 3. Geology of the Kalu'an-Azubai Pegmatite Field

The Kalu'an-Azubai pegmatite field, part of the Kelumute-Jideke district, is located in the Central Altaishan terrane (Figure 1). The exposed stratum is dominated by the middle to late Silurian Kulumuti group that has been metamorphosed and is mainly composed of quartz-biotite schists containing assemblages comprising combinations of muscovite, sillimanite, andalusite, cordierite, staurolite, chlorite, and sericite [3,4]. The protolith of the Kulumuti Group is considered to be a turbiditic sequence that mainly comprises siltstone and sandstone [36]. The Halong granite, which is regarded to be a granitic batholith covering an area of approximately 600 km<sup>2</sup>, is the only exposed granitic pluton in the pegmatite field [4]. The lithology of the granite includes biotite granite and two-mica granite [3].

According to previous studies [2–5], the regional zonation of the pegmatite group mimics that of typical LCT-family pegmatite groups described in London [37]. Four mineralization zones have been divided from the granitic pluton outwards, namely, a zone comprising barren pegmatites (Zone I), a zone dominated by beryl-columbite-phosphate pegmatites (Zone II), a zone of spodumene and lepidolite pegmatites (Zone III), and a quartz vein zone (Zone IV) ([3], Figure 2).

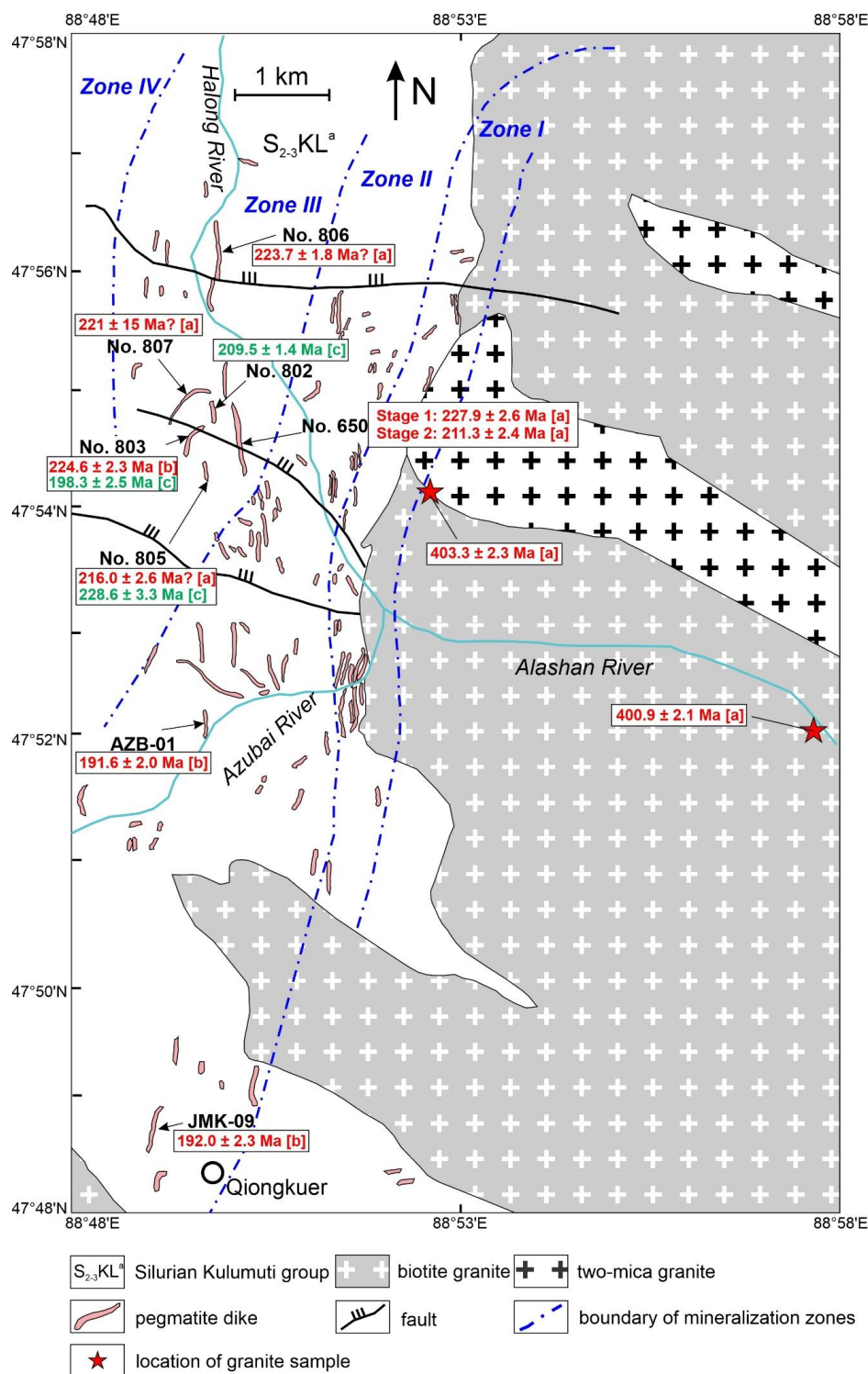


**Figure 2.** Schematic geological map of the Kalu’an-Azubai pegmatite field (after [3]). The age data for the representative Li pegmatites are obtained by (a) Ma et al., 2015 [3], (b) Zhang et al., 2016 [4], (c) this study. On the map, the age data obtained by previous studies are in red color whereas the ages obtained in this study are in green color.

Based on their strikes, the Li pegmatites can be broadly divided into two groups, namely, nearly NS-striking pegmatites (e.g., No. 650, No. 802, and No. 805 pegmatites) and NE to EW-striking pegmatites (e.g., No. 803 and No. 807 pegmatites) (Figure 2). The predominant Li mineral in all Li pegmatites, except No. 650 pegmatite, is spodumene, although lepidolite is present in minor quantities.

No. 650 pegmatite comprises pegmatite dikes formed at two stages [3]. The older pegmatite dike (Stage 1) is composed of quartz and albite with minor spodumene, whereas the younger dike (Stage 2) that crosscuts Stage 1 dike is dominated by quartz, albite, microcline, spodumene, and lepidolite. The Li pegmatites generally consist of two mineralogical zones, namely a medium-to-coarse grained spodumene-albite-quartz zone in which spodumene exhibits obvious orientation (Figure 3a), and an intermediate zone dominated by blocky microcline and quartz (Figure 3b). Spessartine (orange garnet), CGMs, zircon, and beryl are present as accessory minerals in the Li pegmatites. In this study, the CGM-bearing samples were collected from the spodumene-albite-quartz zone. The occurrence, mineralogy and mineralization type of the representative Li pegmatites in the Kalu'an-Azubai region are summarized in Table 1.

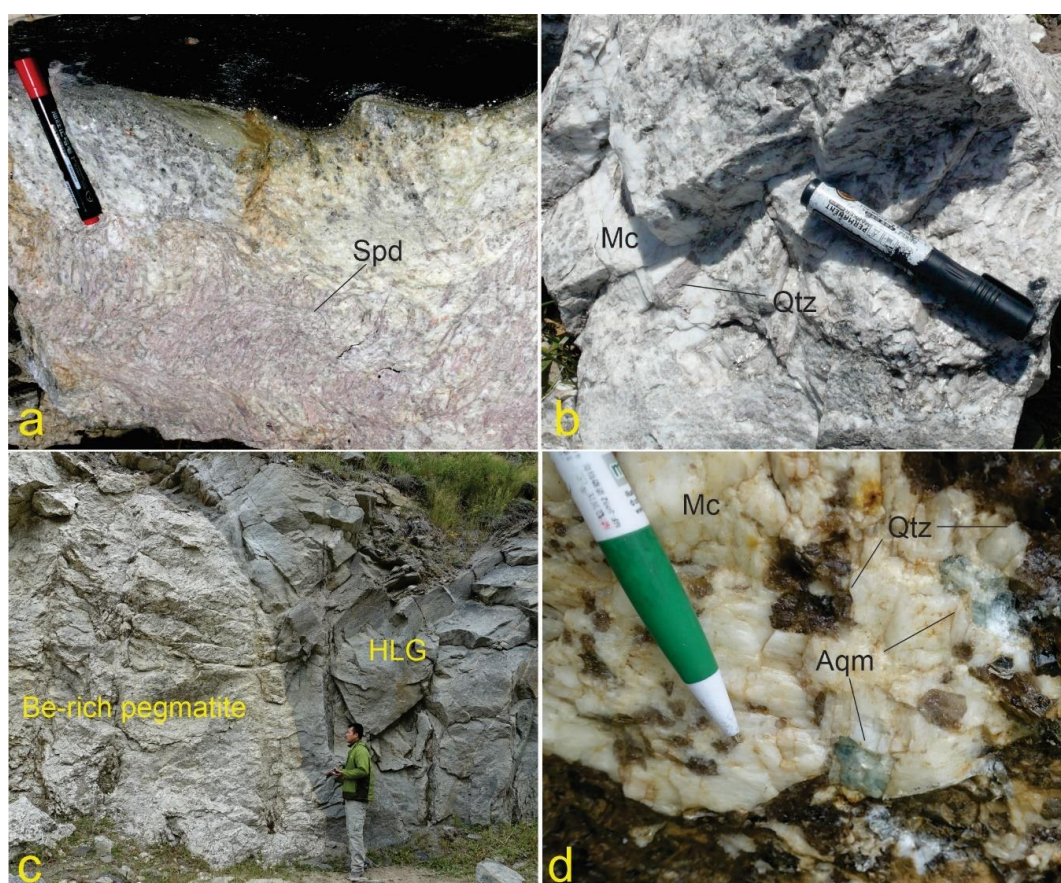


**Figure 3.** Field photos showing typical textures and mineralogy of the Li-rich pegmatites at Kalu'an-Azubai pegmatite field. (a) orientation of pinkish spodumene in the medium- to coarse-grained spodumene-albite-quartz zone and (b) the intermediate zone dominated by blocky microcline and quartz. (c) A Be-rich pegmatite dike intruded into the Halong granite. (d) Coarse-grained aquamarine associated with microcline and quartz in the Be-rich pegmatite. The length of the permanent marker is roughly 15 cm. Abbreviations: Aqm = Aquamarine, Mc = microcline, Qtz = quartz, Spd = spodumene, and HLG = Halong granite.

The Be-(Ta-Nb) pegmatites are mainly composed of quartz, microcline, albite, muscovite, green beryl, aquamarine with minor almandine (reddish garnet), apatite, and triphylite. Aquamarine is mainly distributed in the lithological zone with graphic texture. Locally, triphylite can reach 5–10 vol. % and is associated with garnet. Some Be pegmatite dikes were intruded into the northwestern margin of the Halong granite. Those Be pegmatites exhibit a sharp igneous contact with the biotite granite (Figure 3c) and are mainly composed of quartz, microcline, muscovite, and aquamarine (Figure 3d). Such intrusive contact between Be pegmatites and the Halong granite was not documented in previous studies.

**Table 1.** Geology and ages of representative pegmatite dikes in the Kalu'an-Azubai region.

Pegmatite	Mineralization	Occurrence	Mineralogy	Age (Ma)	References
No. 802	Li	Nearly NS-trending; <100 m long and <3m thick at surface	quartz + microcline + albite + spodumene with lesser muscovite and spessartine	209.5 ± 1.4 <sup>†</sup>	this study
No. 803	Li	NE to EW-trending; approximately 480 m long and 2 m thick	quartz + microcline + albite + spodumene with lesser muscovite and spessartine	198.3 ± 2.0 <sup>†</sup>	this study
No. 805	Li	Nearly NS-trending and E-dipping with a dip angle of ~70°; 90 m long and ~5.5 m thick at surface	quartz + microcline + albite + spodumene with lesser muscovite and spessartine	224.6 ± 2.3 <sup>#</sup>	[4]
No. 806	Li	Nearly NS-trending; 900 m long and 1–5 m thick	quartz + microcline + albite + spodumene with lesser muscovite and spessartine	224.3 ± 2.9 <sup>†</sup>	this study
No. 807	Li	NE to EW-trending and south-dipping with a dip angle of 60–80°; roughly 650 m long	the upper part is dominated by quartz + albite + lepidolite whereas the lower part is dominated by quartz + albite + spodumene	216.0 ± 2.6 <sup>#</sup>	[3]
No. 650	Li	Nearly NS-trending and SW-dipping with a dip angle of 60–70°; 1200 m long and ~10 m thick at surface	Stage 1 pegmatite: quartz + albite with minor spodumene Stage 2 pegmatite: quartz + albite + microcline + spodumene + lepidolite with minor aquamarine	223.7 ± 1.8 <sup>#</sup>	[3]
AZB-01	Be	Nearly NS-trending with a dip angle of ~40°; roughly 450 m long and 3 m wide	quartz + albite + muscovite + microcline + beryl (mostly aquamarine)	227.9 ± 2.6 <sup>#</sup>	[3]
QKE-2-1	Be	This pegmatite crosscuts schist with an irregular contact	quartz + albite + muscovite + microcline + green beryl	211.3 ± 2.4 <sup>†</sup>	[3]
JMK-09	Ta-Nb	NE-trending; approximately 480 m in length and 2–3 m in width with a dip angle of 50°.	quartz + microcline + albite + muscovite with lesser CGM	194.3 ± 1.6 <sup>†</sup>	[5]
				192.0 ± 2.3 <sup>#</sup>	[4]

\*Concordant age obtained using columbite U-Pb dating. †Concordant age obtained using zircon U-Pb dating. #Weighted mean <sup>206</sup>Pb/<sup>238</sup>U age obtained using zircon U-Pb dating.

‡Lower-intercept U-Pb age using zircon U-Pb dating. Note: The errors for the reported zircon U-Pb ages are at 1 sigma whereas those for the columbite U-Pb ages are at 2 sigma.

#### 4. Analytical Methods

Doubly polished thin sections were made for rock samples collected from No. 802, 803, and 805 pegmatites in the Kalu'an-Azubai pegmatite field. Petrographic observations were performed using optical microscopy. Columbite grains were separated from the rock samples, mounted on epoxy resin, and polished for EPMA analysis and LA-ICP-MS dating. An FEI Quanta 650 Environment Scanning Electron Microscopy (ESEM) (Hillsboro, OR, USA) with a mounted INCA EDS (energy dispersive spectroscopy) was used to characterize the internal textures of CGMs at the Laboratory of Mineralization and Dynamics, Chang'an University. The electron beam diameter and accelerating voltage were 5  $\mu\text{m}$  and 15 kV, respectively for BSE imaging. The CGM grains were then analyzed for major element contents using a JEOL JXA-8100 electron microprobe (JEOL, Tokyo, Japan). During EPMA analysis, the accelerating voltage, sample current, and beam diameter were 15 kV, 15 nA, and 2  $\mu\text{m}$ , respectively. The working condition of EPMA analysis is summarized in Supplementary Material Table S1. The analytical precision for major element oxide contents >1 wt.% is better than 3% (expressed as relative standard deviation). Summary of EPMA data for CGMs is given in Table 2. The complete EPMA dataset for CGMs is given in Supplementary Material Table S2.

Columbite U-Pb dating was performed using a Thermo Fisher Scientific iCAP-Q model ICP-MS (Thermo Fisher Scientific, Waltham, MA, USA) coupled with a RESOLUTION S155 193 nm ArF excimer laser ablation system at the State Key Laboratory for Mineral Deposits Research, Nanjing University. The diameter and energy of the laser beam were 43  $\mu\text{m}$  and  $1.2 \times 10^3 \text{ mJ/cm}^2$ , respectively. The repetition rate of laser pulses was set to 4 Hz. Coltan 139 with a weighted mean  $^{207}\text{Pb}/^{206}\text{Pb}$  age of  $506 \pm 2.3 \text{ Ma}$  (obtained by ID-TIMS) and an LA-ICP-MS U-Pb age of  $506.2 \pm 5.0 \text{ Ma}$  ([14] and references therein) was used as the external standard for calibrating U, Th, Pb isotopic ratios. No secondary standards were used due to lack of suitable CGM standards. However, Che et al. [14] showed that no matrix effect as a function of columbite compositions occurred during LA-ICP-MS dating. Therefore, it was assumed that the standard and unknowns were matrix-matched, and that laser-target induced bias was minimal. Meanwhile, zircon standards 91500 and PL were used for monitoring the signals of U, Th, and Pb isotopes. Time for collecting gas background signals and signals from samples or standards were 20 s and 50 s, respectively. Readers are referred to Che et al. [14] for the detailed descriptions of the analytical procedure. Software Iolite [38] and Isoplot 3.0 [39] were used to calculate the ratios of  $^{206}\text{Pb}/^{238}\text{U}$ ,  $^{207}\text{Pb}/^{235}\text{U}$ ,  $^{207}\text{Pb}/^{206}\text{Pb}$ , and  $^{208}\text{Pb}/^{232}\text{Th}$ , to process age data, respectively. Common Pb correction was not needed because of the extremely low common Pb ( $^{204}\text{Pb}$ ) concentrations in CGM, as indicated by  $^{206}\text{Pb}/^{204}\text{Pb}$  ratios (Table 3). The dating results are given in Table 3. The BSE images showing all the analytical spots for columbite LA-ICP-MS dating are given in Supplementary Material Figure S1. After LA-ICP-MS dating, the analyzed CGM grains were examined using SEM for age data screening. The working condition for the SEM-EDS analysis was similar to that for BSE imaging prior to EPMA and LA-ICP-MS analyses.

The dated CGM grains were polished, cleaned, and analyzed for trace element concentrations using a Photon Machines 193 nm excimer laser ablation system coupled with an Agilent 7700 ICP-MS (Santa Clara, CA, USA) at Chang'an University. The analyzed elemental isotopes included  $^{44}\text{Ca}$ ,  $^{45}\text{Sc}$ ,  $^{55}\text{Mn}$ ,  $^{89}\text{Y}$ ,  $^{90}\text{Zr}$ ,  $^{93}\text{Nb}$ ,  $^{118}\text{Sn}$ ,  $^{139}\text{La}$ ,  $^{140}\text{Ce}$ ,  $^{141}\text{Pr}$ ,  $^{146}\text{Nd}$ ,  $^{147}\text{Sm}$ ,  $^{149}\text{Sm}$ ,  $^{153}\text{Eu}$ ,  $^{157}\text{Gd}$ ,  $^{159}\text{Tb}$ ,  $^{163}\text{Dy}$ ,  $^{165}\text{Ho}$ ,  $^{166}\text{Er}$ ,  $^{169}\text{Tm}$ ,  $^{172}\text{Yb}$ ,  $^{175}\text{Lu}$ ,  $^{177}\text{Hf}$ ,  $^{182}\text{W}$ ,  $^{206}\text{Pb}$ ,  $^{232}\text{Th}$ , and  $^{238}\text{U}$ . Helium gas was the carrier gas. The diameter, energy density, and repetition rate of the laser beam were 25  $\mu\text{m}$ ,  $6.75 \times 10^3 \text{ mJ/cm}^2$ , and 10 Hz, respectively. For each analysis, signals on the gas background and sample were collected for 10 s and 40 s, respectively. The analytical procedure and the method for the precision test were described in Feng et al. [40]. NIST SRM 610 and NIST SRM 612 were used as the primary and secondary external standards. Software Iolite was used to calculate trace element concentrations. The EPMA analysis indicates that the oscillatory zoning of the CGMs is caused by Ta oscillation and that the MnO contents are fairly consistent across the individual CGM grains (see Section 5.2). Therefore,  $^{55}\text{Mn}$  was used as the internal standard. The Mn concentrations were based on the EPMA analysis on the same spots for LA-ICP-MS analysis or next to the ablation pits. The results are summarized in Table 4. The information regarding the precision and detection limits and the complete dataset of trace element concentrations are provided in Supplementary Material Table S3.

**Table 2.** Summary of chemical compositions of columbite-tantalite group minerals (CGMs) from the Li pegmatites at Kalu'an.

Element (wt.%)	No. 802 Pegmatite						No. 803 Pegmatite				
	Core		Middle		Rim		Core		Nb-Rich Middle		Ta-Rich Middle
	Mean (n = 35)	sd	Mean (n = 5)	sd	Mean (n = 9)	sd	Mean (n = 29)	sd	Mean (n = 6)	sd	Mean (n = 4)
Al <sub>2</sub> O <sub>3</sub>	0.03	0.02	0.02	0.01	0.03	0.02	0.03	0.01	0.04	0.03	0.32
WO <sub>3</sub>	0.12	0.07	b.d.	n.a.	0.12	n.a.	0.24	0.17	0.05	0.06	b.d.
TiO <sub>2</sub>	0.25	0.07	0.26	0.18	0.28	0.09	0.36	0.18	0.47	0.30	0.32
Ta <sub>2</sub> O <sub>5</sub>	16.65	3.75	44.45	3.85	23.83	2.87	21.60	4.73	21.10	5.41	48.62
Sc <sub>2</sub> O <sub>3</sub>	0.09	0.03	0.26	0.04	0.14	0.03	0.12	0.04	0.12	0.03	0.29
FeO <sub>t</sub>	0.96	0.48	1.07	0.59	1.06	0.46	0.97	0.61	1.57	0.68	0.90
CaO	0.01	0.01	0.01	0.01	0.01	0.01	0.01	0.01	0.02	0.01	0.02
MnO	15.61	0.58	13.71	0.42	14.92	0.33	15.28	0.67	15.00	0.52	13.31
SnO <sub>2</sub>	0.03	0.01	0.02	0.01	0.03	0.02	0.02	0.01	0.01	0.02	b.d.
Nb <sub>2</sub> O <sub>5</sub>	63.89	3.77	35.53	4.29	56.03	3.18	58.68	4.75	59.19	4.82	31.43
Total	97.50	1.26	95.32	1.01	96.31	0.76	97.18	1.19	97.52	1.20	95.21
apfu	based on 6 oxygen atoms										
W	0.000	0.001	0.000	0.000	0.000	0.001	0.002	0.003	0.000	0.001	0.000
Ti	0.012	0.003	0.014	0.010	0.013	0.004	0.017	0.008	0.022	0.014	0.017
Al	0.002	0.002	0.001	0.001	0.002	0.002	0.001	0.001	0.003	0.002	0.029
Ta	0.279	0.070	0.874	0.101	0.418	0.058	0.373	0.090	0.363	0.099	0.986
Sc	0.005	0.002	0.017	0.003	0.008	0.002	0.007	0.002	0.006	0.002	0.019
Fe	0.049	0.025	0.064	0.034	0.057	0.024	0.052	0.033	0.082	0.036	0.055
Ca	0.000	0.001	0.000	0.000	0.001	0.001	0.001	0.001	0.001	0.001	0.001
Mn	0.812	0.025	0.838	0.038	0.813	0.027	0.817	0.030	0.799	0.024	0.836
Sn	0.000	0.000	0.000	0.000	0.000	0.000	0.000	0.000	0.000	0.000	0.000
Nb	1.773	0.073	1.155	0.106	1.629	0.062	1.672	0.092	1.680	0.101	1.045
Nb/Ta	6.7	1.5	1.3	0.3	4.0	0.7	4.8	1.6	5.3	2.2	1.1
#Mn	94.3	2.9	92.9	3.8	93.5	2.8	94.1	3.7	90.7	3.9	93.8
#Ta	13.6	3.4	43.1	5.1	20.4	2.9	18.2	4.4	17.8	4.9	48.6

Table 2. Cont.

Element (wt.%)	No. 803 Pegmatite						No. 805 Pegmatite					
	Ta-Rich Middle sd	Rim		CGM-I, Core		CGM-I, Middle		CGM-I, Rim		CGM-II		
		mean (n = 29)	sd	mean (n = 12)	sd	mean (n = 34)	sd	mean (n = 11)	sd	mean (n = 4)	sd	
Al <sub>2</sub> O <sub>3</sub>	0.56	0.07	0.21	0.02	0.01	0.03	0.02	0.02	0.01	0.04	0.01	
WO <sub>3</sub>	b.d.	0.20	0.17	0.33	0.20	0.12	n.a.	b.d.	n.a.	b.d.	n.a.	
TiO <sub>2</sub>	0.21	0.36	0.14	0.21	0.13	0.13	0.07	0.16	0.08	0.26	0.08	
Ta <sub>2</sub> O <sub>5</sub>	7.50	21.57	3.56	17.93	3.40	33.60	4.68	71.39	4.33	20.97	6.53	
Sc <sub>2</sub> O <sub>3</sub>	0.06	0.12	0.03	0.09	0.03	0.18	0.04	0.39	0.05	0.10	0.05	
FeO <sub>t</sub>	0.45	1.03	0.58	1.46	0.69	1.34	0.36	1.05	0.34	2.05	0.60	
CaO	0.00	0.02	0.01	0.02	0.02	0.02	0.01	0.01	0.01	0.01	0.02	
MnO	0.38	15.12	0.58	15.23	0.81	14.27	0.50	11.98	0.38	14.65	0.47	
SnO <sub>2</sub>	n.a.	0.03	0.03	0.02	0.02	0.02	0.02	0.04	0.00	0.04	n.a.	
Nb <sub>2</sub> O <sub>5</sub>	7.59	58.45	3.65	61.90	4.34	47.32	4.81	11.03	4.20	60.08	6.39	
Total	1.08	96.86	1.13	96.97	1.88	96.89	1.05	96.03	1.14	98.17	0.46	
apfu	based on 6 oxygen atoms											
W	0.000	0.002	0.003	0.002	0.003	0.000	0.000	0.000	0.000	0.000	0.000	
Ti	0.011	0.017	0.007	0.010	0.006	0.007	0.003	0.010	0.005	0.012	0.004	
Al	0.051	0.004	0.013	0.001	0.001	0.002	0.002	0.002	0.001	0.003	0.001	
Ta	0.197	0.373	0.069	0.305	0.068	0.613	0.103	1.609	0.142	0.358	0.118	
Sc	0.005	0.007	0.002	0.005	0.002	0.010	0.002	0.028	0.004	0.006	0.003	
Fe	0.026	0.055	0.031	0.076	0.036	0.075	0.020	0.072	0.022	0.106	0.030	
Ca	0.001	0.001	0.001	0.001	0.001	0.001	0.001	0.001	0.001	0.001	0.001	
Mn	0.040	0.812	0.030	0.802	0.036	0.808	0.027	0.840	0.026	0.772	0.037	
Sn	0.000	0.000	0.001	0.000	0.000	0.000	0.000	0.000	0.000	0.000	0.001	
Nb	0.205	1.673	0.072	1.738	0.070	1.427	0.106	0.409	0.145	1.687	0.124	
Nb/Ta	0.4	4.7	1.0	6.0	1.6	2.4	0.6	0.3	0.1	5.5	3.2	
#Mn	3.0	93.7	3.5	91.4	4.1	91.5	2.3	92.1	2.4	87.9	3.5	
#Ta	9.9	18.2	3.4	14.9	3.3	30.1	5.1	79.8	7.1	17.5	5.8	

Note: #Mn and #Ta are molar ratios of  $100 \times \text{Mn}/(\text{Mn} + \text{Fe})$  and  $100 \times \text{Ta}/(\text{Ta} + \text{Nb})$ , respectively (cf. [41]). Abbreviations: “sd” = “standard deviation”, “apfu” = “atoms per formula unit”, “n” = number of analyses, “b.d.” = “below detection limit”, and “n.a.” = “not available”. “FeO<sub>t</sub>” = “FeO total”.

**Table 3.** Results of columbite LA-ICP-MS (laser ablation-inductively coupled plasma mass spectrometer) dating for the Kalu'an Li-rich pegmatites.

Analysis#	U (ppm)	Th (ppm)	<sup>206</sup> Pb/ <sup>204</sup> Pb	<sup>207</sup> Pb/ <sup>235</sup> U	2σ	Isotopic Ratios						Age (Ma)			Concordance	
						<sup>206</sup> Pb/ <sup>238</sup> U	2σ	<sup>207</sup> Pb/ <sup>206</sup> Pb	2σ	<sup>207</sup> Pb/ <sup>235</sup> U	2σ	<sup>206</sup> Pb/ <sup>238</sup> U	2σ	<sup>207</sup> Pb/ <sup>206</sup> Pb		2σ
<b>No. 802 Pegmatite</b>																
K802.1	1043.0	37.9	1490	0.2303	0.005	0.03287	0.0003	0.0517	0.0011	210.0	4.1	208.5	2.0	249.0	45.0	99.28%
K802.2	330.4	14.7	1740	0.2227	0.006	0.03302	0.0004	0.0523	0.0013	203.8	4.7	209.4	2.6	273.0	53.0	97.33%
K802.3	470.0	14.9	1740	0.2343	0.007	0.0332	0.0005	0.0523	0.0015	213.2	5.8	210.5	3.1	266.0	63.0	98.72%
K802.4	223.5	6.9	1230	0.2153	0.0086	0.03342	0.0008	0.0505	0.0021	198.7	7.5	211.9	4.7	190.0	85.0	93.77%
K802.5	405.0	11.5	3100	0.2372	0.006	0.03328	0.0005	0.0504	0.0011	216.6	4.8	211.0	3.0	201.0	50.0	97.35%
K802.6	277.6	8.0	640	0.2304	0.0066	0.03469	0.0005	0.0521	0.0014	211.6	5.4	219.8	3.2	275.0	58.0	96.27%
K802.7	347.1	9.4	1020	0.2515	0.0076	0.033	0.0005	0.0549	0.0018	228.1	6.4	209.3	3.3	377.0	73.0	91.02%
K802.8	364.5	11.7	1570	0.2329	0.007	0.03328	0.0005	0.0507	0.0013	211.8	5.8	211.0	3.1	201.0	56.0	99.62%
K802.9	590.0	20.4	1530	0.2282	0.008	0.0327	0.0006	0.051	0.0020	208.3	6.7	207.4	3.7	216.0	83.0	99.57%
K802.10	335.0	8.8	1680	0.247	0.011	0.03346	0.0006	0.0521	0.0024	225.1	9.4	212.2	3.9	270.0	100.0	93.92%
K802.11	291.0	10.7	1490	0.2571	0.0096	0.03397	0.0007	0.0532	0.0021	231.8	7.8	215.3	4.3	299.0	87.0	92.34%
K802.12	353.1	9.8	1690	0.2491	0.008	0.03423	0.0006	0.0515	0.0014	225.2	6.5	216.9	4.0	246.0	62.0	96.17%
K802.13	713.0	21.0	2920	0.2287	0.004	0.03326	0.0003	0.05123	0.0008	208.8	3.0	210.9	2.1	234.0	34.0	99.00%
K802.14	1016.9	29.5	3700	0.2348	0.006	0.03282	0.0005	0.0502	0.0013	213.9	4.6	208.1	3.3	190.0	57.0	97.21%
K802.15	287.0	8.8	1790	0.241	0.019	0.03271	0.0009	0.0507	0.0040	218.0	16.0	207.5	5.5	200.0	170.0	94.94%
K802.16	409.0	13.6	2130	0.2315	0.006	0.03291	0.0004	0.051	0.0013	211.0	4.5	208.7	2.7	214.0	53.0	98.90%
K802.17	392.0	10.4	1900	0.248	0.012	0.03259	0.0007	0.0524	0.0026	225.0	10.0	206.7	4.6	280.0	110.0	91.15%
K802.18	671.0	15.7	1500	0.262	0.016	0.03369	0.0010	0.0544	0.0034	235.0	13.0	213.6	6.0	330.0	130.0	89.98%
K802.19	454.0	13.3	6600	0.235	0.005	0.03283	0.0004	0.0517	0.0011	214.0	4.3	208.2	2.6	251.0	47.0	97.21%
K802.20	275.3	7.1	1600	0.2442	0.0082	0.03293	0.0006	0.054	0.0019	221.1	6.7	208.8	3.4	329.0	76.0	94.11%
K802.21	224.0	7.6	2400	0.258	0.015	0.03276	0.0009	0.0551	0.0034	232.0	12.0	207.8	5.4	360.0	140.0	88.35%
K802.22	277.0	6.8	1300	0.2323	0.007	0.03316	0.0004	0.0512	0.0016	211.4	5.6	210.3	2.7	221.0	65.0	99.48%
K802.23	299.0	8.6	1400	0.255	0.011	0.03391	0.0007	0.0528	0.0021	229.6	8.9	214.9	4.3	305.0	92.0	93.16%
K802.24	324.0	11.5	200	0.2397	0.008	0.03301	0.0005	0.0518	0.0017	217.5	6.2	209.3	2.8	236.0	70.0	96.08%
K802.25	245.0	7.1	1900	0.23	0.011	0.03267	0.0006	0.0514	0.0026	209.4	9.4	207.2	4.0	220.0	100.0	98.94%
K802.26	360.0	10.2	1400	0.237	0.012	0.03404	0.0007	0.0497	0.0028	215.0	10.0	215.7	4.4	140.0	110.0	99.68%
K802.27	222.3	6.7	1500	0.256	0.013	0.03396	0.0009	0.0532	0.0027	230.0	11.0	215.3	5.4	310.0	110.0	93.17%
K802.28	532.0	16.0	530	0.2436	0.008	0.03388	0.0006	0.0518	0.0018	221.5	7.0	214.8	3.6	238.0	74.0	96.88%
K802.29	322.0	8.8	250	0.247	0.011	0.03363	0.0006	0.0533	0.0023	223.3	8.7	213.2	4.0	294.0	94.0	95.26%

Table 3. Cont.

Analysis#	U (ppm)	Th (ppm)	<sup>206</sup> Pb/ <sup>204</sup> Pb	<sup>207</sup> Pb/ <sup>235</sup> U	2σ	Isotopic Ratios						Age (Ma)			Concordance	
						<sup>206</sup> Pb/ <sup>238</sup> U	2σ	<sup>207</sup> Pb/ <sup>206</sup> Pb	2σ	<sup>207</sup> Pb/ <sup>235</sup> U	2σ	<sup>206</sup> Pb/ <sup>238</sup> U	2σ	<sup>207</sup> Pb/ <sup>206</sup> Pb		2σ
<b>No. 803 pegmatite</b>																
K803.1	1870.0	94.0	1310	0.209	0.005	0.02949	0.0005	0.05111	0.0010	192.3	4.3	187.3	3.2	231.0	43.0	97.33%
K803.2	159.8	5.3	560	0.2342	0.0081	0.0316	0.0005	0.0538	0.0017	212.3	6.7	200.5	2.9	305.0	66.0	94.11%
K803.3	537.0	20.9	1850	0.2235	0.007	0.03094	0.0005	0.0515	0.0017	204.4	5.8	196.4	2.9	238.0	71.0	95.93%
K803.4	573.6	29.3	1820	0.2205	0.008	0.03113	0.0006	0.0514	0.0019	201.9	6.6	197.6	4.0	232.0	82.0	97.82%
K803.5	745.4	32.4	2080	0.2172	0.006	0.03124	0.0006	0.0504	0.0013	199.3	5.3	198.3	3.8	208.0	58.0	99.50%
K803.6	756.3	34.6	2190	0.2186	0.003	0.03149	0.0003	0.05033	0.0008	200.5	2.8	199.9	1.9	200.0	36.0	99.70%
K803.7	942.0	33.2	1270	0.2232	0.007	0.0311	0.0005	0.0507	0.0015	204.0	5.5	197.4	2.8	199.0	63.0	96.66%
K803.8	516.0	13.1	1740	0.2177	0.004	0.03084	0.0004	0.0511	0.0008	199.5	3.1	195.8	2.2	228.0	36.0	98.11%
K803.9	442.8	16.9	1900	0.2202	0.0044	0.03014	0.0003	0.0528	0.0011	201.5	3.7	191.4	1.7	281.0	43.0	94.72%
K803.10	1812.8	89.8	9900	0.2469	0.0033	0.03259	0.0004	0.05473	0.0005	223.8	2.7	206.7	2.5	390.0	21.0	91.73%
K803.11	303.3	12.1	960	0.2433	0.0054	0.03337	0.0004	0.0528	0.0012	220.3	4.4	211.6	2.3	287.0	48.0	95.89%
K803.12	840.0	36.1	4420	0.2119	0.003	0.03079	0.0003	0.04991	0.0006	194.9	2.4	195.5	1.9	179.0	27.0	99.69%
K803.13	1156.1	65.1	5100	0.2183	0.005	0.03117	0.0005	0.05131	0.0008	200.3	3.8	197.8	3.2	243.0	37.0	98.74%
K803.14	221.0	7.7	2450	0.2233	0.005	0.03191	0.0004	0.05092	0.0010	204.2	3.8	202.5	2.5	213.0	42.0	99.16%
K803.15	671.0	20.3	3400	0.2164	0.005	0.03174	0.0004	0.04987	0.0009	199.0	3.9	201.4	2.7	177.0	41.0	98.81%
K803.16	533.0	26.8	2570	0.2471	0.0046	0.03289	0.0003	0.0545	0.0010	223.8	3.7	208.8	2.2	367.0	41.0	92.82%
K803.17	1466.6	67.7	7400	0.2158	0.003	0.0312	0.0003	0.05027	0.0005	198.5	2.1	198.1	1.6	197.0	24.0	99.80%
K803.18	279.0	11.5	1500	0.2365	0.0056	0.0312	0.0004	0.0554	0.0013	215.3	4.6	198.0	2.6	390.0	51.0	91.26%
K803.19	356.0	12.6	1550	0.2291	0.0065	0.03056	0.0004	0.0549	0.0016	208.9	5.4	194.0	2.6	366.0	65.0	92.32%
K803.20	305.3	15.0	1260	0.2142	0.007	0.03045	0.0005	0.0512	0.0015	196.4	5.7	193.3	3.1	220.0	62.0	98.40%
K803.21	387.3	16.8	1390	0.2129	0.005	0.03046	0.0004	0.0512	0.0012	195.4	4.0	193.4	2.3	221.0	49.0	98.97%
K803.22	528.9	27.7	2450	0.2148	0.0032	0.03008	0.0002	0.05188	0.0008	197.4	2.7	191.0	1.5	260.0	34.0	96.65%
K803.23	566.8	19.6	2580	0.2224	0.007	0.03191	0.0006	0.0509	0.0014	203.4	5.6	202.5	3.7	212.0	61.0	99.56%
K803.24	1068.0	61.8	5100	0.212	0.003	0.03047	0.0003	0.0507	0.0007	195.0	2.6	193.5	2.0	215.0	29.0	99.22%
K803.25	786.9	37.9	3780	0.2214	0.003	0.03131	0.0003	0.05131	0.0006	202.8	2.5	198.7	1.9	243.0	28.0	97.94%
K803.26	1322.2	83.8	7100	0.2179	0.003	0.03079	0.0003	0.0516	0.0007	200.2	2.5	195.5	2.0	255.0	30.0	97.60%
K803.27	1249.4	69.2	6100	0.2206	0.005	0.03139	0.0005	0.0511	0.0010	202.2	3.9	199.2	3.0	227.0	45.0	98.49%
K803.28	581.3	27.7	2500	0.2305	0.0037	0.0309	0.0003	0.05426	0.0008	210.5	3.1	196.2	1.7	357.0	34.0	92.71%
K803.29	327.4	13.9	1630	0.2191	0.004	0.03118	0.0003	0.05102	0.0010	200.8	3.7	197.9	1.9	213.0	41.0	98.53%

Table 3. Cont.

Analysis#	U (ppm)	Th (ppm)	<sup>206</sup> Pb/ <sup>204</sup> Pb	<sup>207</sup> Pb/ <sup>235</sup> U	2σ	Isotopic Ratios						Age (Ma)			Concordance	
						<sup>206</sup> Pb/ <sup>238</sup> U	2σ	<sup>207</sup> Pb/ <sup>206</sup> Pb	2σ	<sup>207</sup> Pb/ <sup>235</sup> U	2σ	<sup>206</sup> Pb/ <sup>238</sup> U	2σ	<sup>207</sup> Pb/ <sup>206</sup> Pb		2σ
No. 805 pegmatite																
K805.1	662.0	14.4	3200	0.2663	0.0049	0.03607	0.0004	0.05137	0.0008	239.2	3.9	228.4	2.2	240.0	37.0	95.27%
K805.2	756.0	19.9	1580	0.2618	0.0069	0.03512	0.0005	0.0521	0.0013	235.2	5.5	222.5	2.9	259.0	54.0	94.29%
K805.3	320.2	10.9	1040	0.256	0.0074	0.03464	0.0006	0.0529	0.0016	230.7	5.9	219.5	3.8	282.0	63.0	94.90%
K805.4	342.2	6.3	2060	0.262	0.014	0.0352	0.0013	0.0548	0.0026	235.0	11.0	223.1	7.9	380.0	110.0	94.67%
K805.5	216.0	4.7	1530	0.2557	0.009	0.03547	0.0006	0.0526	0.0017	230.3	6.9	224.6	3.8	271.0	70.0	97.46%
K805.6	139.7	3.1	700	0.263	0.016	0.03496	0.0009	0.0546	0.0035	235.0	13.0	221.5	5.7	310.0	130.0	93.91%
K805.7	142.0	5.6	980	0.2794	0.0068	0.03625	0.0005	0.054	0.0013	248.8	5.4	229.5	2.9	310.0	51.0	91.59%
K805.8	176.0	3.9	380	0.251	0.011	0.0366	0.0010	0.0514	0.0026	226.4	9.3	231.4	6.3	210.0	100.0	97.84%
K805.9	400.5	15.0	1540	0.2688	0.009	0.03548	0.0007	0.0509	0.0015	240.8	7.2	224.7	4.2	215.0	64.0	92.83%
K805.10	208.0	4.6	2020	0.2579	0.007	0.03599	0.0006	0.0529	0.0013	232.5	5.9	227.9	4.0	298.0	55.0	97.98%
K805.11	1053.5	31.7	4500	0.2521	0.007	0.03466	0.0006	0.0515	0.0011	227.8	5.7	219.6	3.8	254.0	47.0	96.27%
K805.12	237.8	8.5	1040	0.257	0.01	0.03429	0.0006	0.0526	0.0020	231.1	8.1	217.3	4.0	263.0	78.0	93.65%
K805.13	493.8	16.5	1900	0.25	0.011	0.03509	0.0009	0.052	0.0022	225.5	8.9	222.3	5.5	252.0	91.0	98.56%
K805.14	230.0	6.2	970	0.269	0.014	0.0355	0.0012	0.0556	0.0027	241.0	11.0	224.7	7.4	380.0	110.0	92.75%
K805.15	366.0	8.8	1020	0.273	0.015	0.0352	0.0011	0.057	0.0031	243.0	12.0	223.1	6.7	420.0	120.0	91.08%
K805.16	314.0	6.7	1100	0.263	0.015	0.0352	0.0012	0.0546	0.0031	236.0	12.0	222.9	7.2	350.0	120.0	94.12%
K805.17	384.5	13.5	1880	0.2521	0.005	0.03569	0.0004	0.0519	0.0011	227.9	4.2	226.2	2.2	246.0	44.0	99.25%
K805.18	385.6	13.4	1130	0.267	0.011	0.0353	0.0009	0.0551	0.0021	239.1	9.1	223.6	5.6	389.0	81.0	93.07%
K805.19	271.2	6.3	1160	0.2604	0.0068	0.03595	0.0005	0.0533	0.0013	233.9	5.4	227.6	3.1	300.0	51.0	97.23%
K805.20	217.3	4.5	530	0.26	0.011	0.03503	0.0006	0.0535	0.0020	234.4	9.1	221.9	4.0	347.0	83.0	94.37%
K805.21	247.9	7.7	1760	0.2553	0.01	0.03532	0.0008	0.0532	0.0019	230.1	7.8	223.7	4.9	301.0	78.0	97.14%
K805.22	627.4	21.8	1800	0.2486	0.007	0.03507	0.0005	0.0518	0.0014	225.0	5.3	222.2	3.3	250.0	57.0	98.74%
K805.23	436.8	18.6	1310	0.2544	0.0098	0.03491	0.0007	0.0532	0.0019	229.5	8.0	221.2	4.4	317.0	74.0	96.25%
K805.24	182.7	4.2	840	0.27	0.012	0.03607	0.0009	0.055	0.0026	241.1	9.8	228.4	5.4	360.0	100.0	94.44%
K805.25	594.0	13.1	3400	0.2598	0.009	0.0359	0.0011	0.0529	0.0017	233.9	7.5	227.3	6.6	297.0	73.0	97.10%
K805.26	235.6	5.3	520	0.266	0.019	0.0355	0.0010	0.0547	0.0036	237.0	15.0	224.7	6.5	320.0	140.0	94.53%
K805.27	599.0	16.1	140	0.269	0.017	0.0359	0.0011	0.055	0.0036	241.0	13.0	227.1	7.0	340.0	140.0	93.88%

Note: the analyses with bold text were selected for Concordia age calculation.

## 5. Results

### 5.1. Petrography

Petrographic observations reveal that CGMs in all the three investigated pegmatites mainly occur in the spodumene-albite-quartz zone and show planar contact with spodumene and muscovite (Figure 4). Columbite-group minerals are generally euhedral to subhedral and reddish-brown in plane-polarized transmitted light. The grain size of CGMs mainly varies between 100  $\mu\text{m}$  and 300  $\mu\text{m}$ .

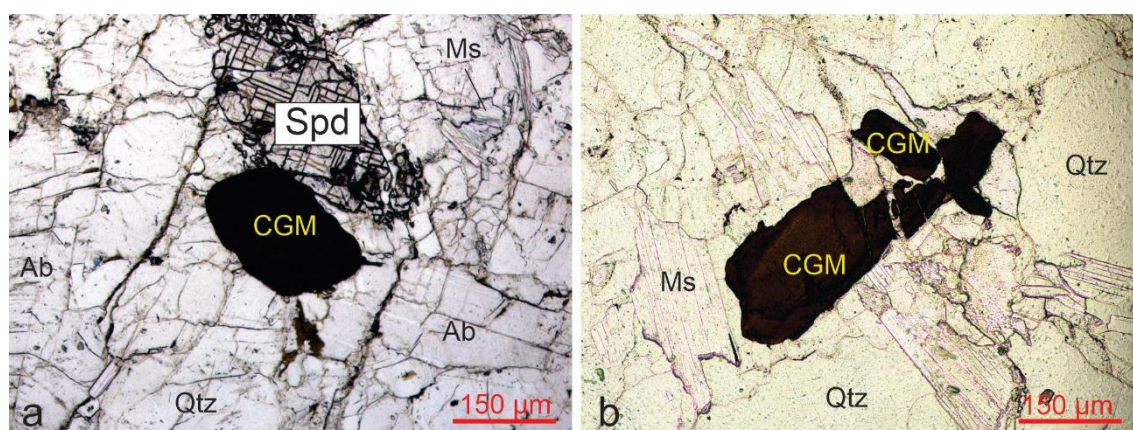


**Figure 4.** Photomicrographs showing typical CGM-bearing mineral assemblages in the investigated Li-rich pegmatites at Kalu'an. (a) coexisting CGM and spodumene that are associated with quartz, albite, and muscovite, (b) CGM associated with quartz and muscovite. Both photomicrographs were taken in plane-polarized transmitted light. Abbreviations: Ab = albite, CGM = columbite-group mineral, Ms = muscovite, Spd = spodumene, and Qtz = quartz.

Backscattered electron imaging shows that the majority of CGMs exhibit either oscillatory zoning or sector zoning or both (Figure 5). In No. 802 pegmatite, the core and rim of well-zoned CGMs are generally grey whereas the middle part appears bright on BSE images (e.g., CGM grain K802.5 and K802.29 in Figure 5). The CGMs in No. 803 pegmatite show relatively complicated brightness variation on BSE images compared with the CGMs in No. 802 pegmatite (Figure 5). The CGMs in No. 805 pegmatite can be divided into two generations based on BSE imaging, namely a primary phase (CGM-I) with prominent oscillatory zoning and a secondary dark phase (CGM-II) that replaces CGM-I (Figure 5). Overall, the brightness increases from the core to the rim of CGM-I on BSE images.

### 5.2. EPMA

All the analyzed CGMs contain <3 wt.%  $\text{FeO}_t$ , 11.3–16.2 wt.%  $\text{MnO}$ , and 0.18–0.5 wt.%  $\text{TiO}_2$ . The  $\text{Al}_2\text{O}_3$ ,  $\text{CaO}$ ,  $\text{Sc}_2\text{O}_3$ ,  $\text{WO}_3$ , and  $\text{SnO}_2$  contents are mostly below 0.5 wt.% (Table 2). By contrast, the  $\text{Nb}_2\text{O}_5$  and  $\text{Ta}_2\text{O}_5$  contents are variable. All the analyzed CGMs (except the rim of CGM-I from No. 805 pegmatite) are compositionally columbite-(Mn) (Table 2, Figure 6).

In No. 802 pegmatite, the core, middle, and rim of the CGMs show comparable #Mn values (mostly varying between 90 and 95) but variable #Ta values. The #Ta values ( $43.1 \pm 5.1$ ) of the middle are much higher than that of the core and rim (Figure 6).

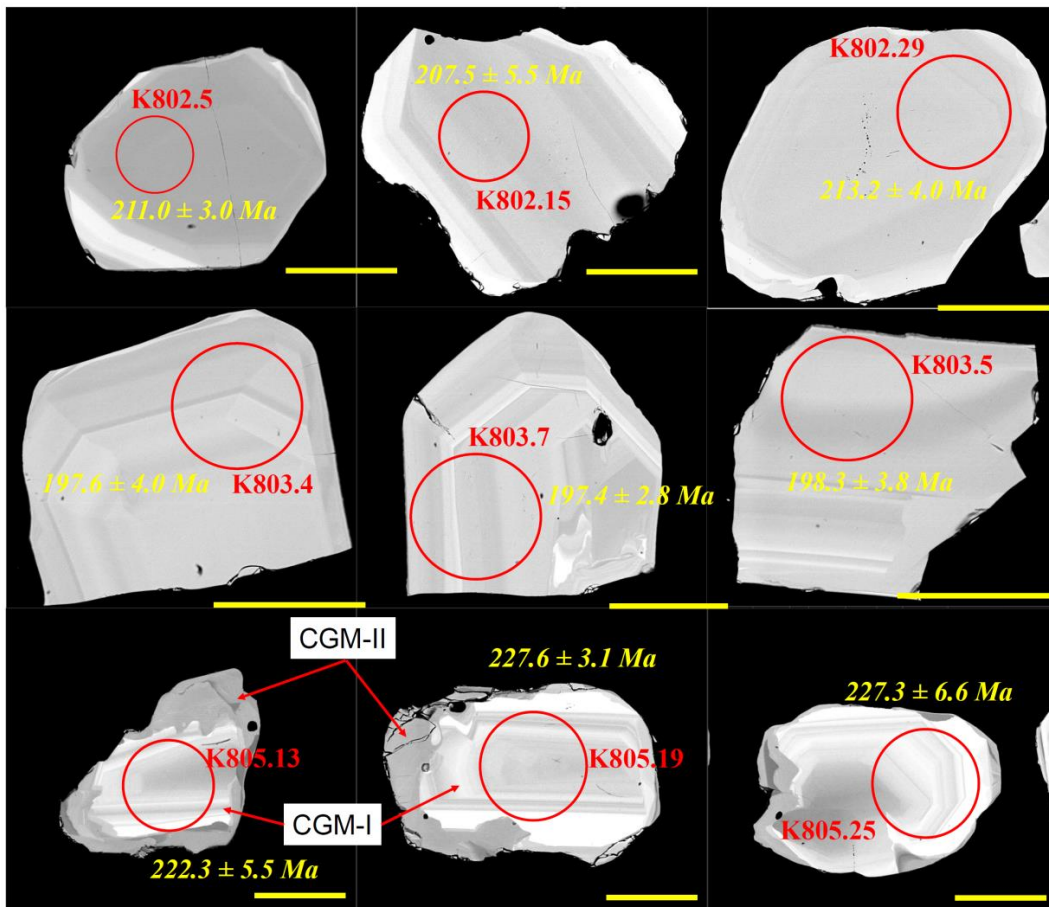


**Figure 5.** BSE images of representative CGM grains from No. 802, No. 803, and No. 805 pegmatites at Kalu'an in the Chinese Altay orogen. The red circles represent the positions of ablation pits during LA-ICP-MS dating and the relevant apparent  $^{206}\text{Pb}/^{238}\text{U}$  ages are shown next to individual ablation pits. All the scale bars are 50  $\mu\text{m}$  long.

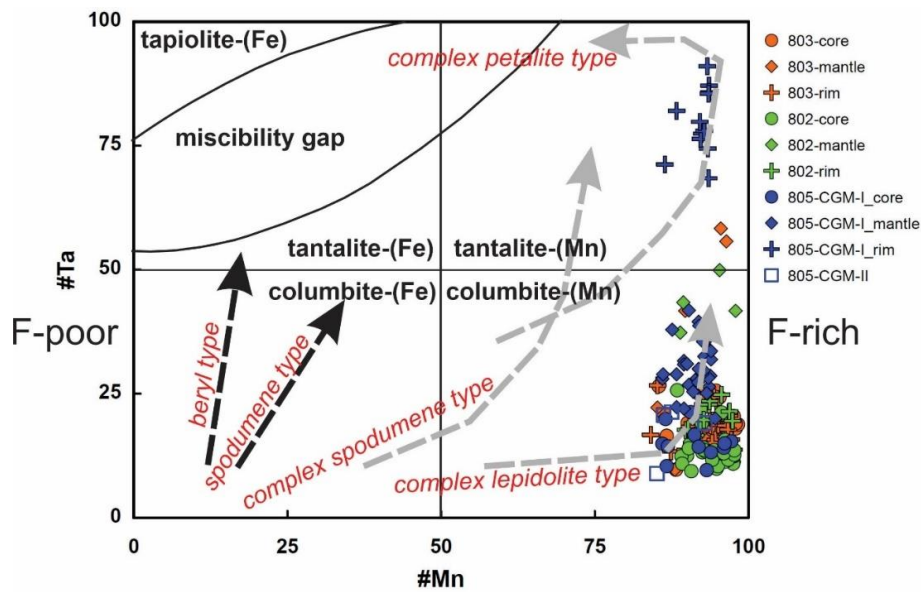


**Figure 6.** #Ta-#Mn quadrilateral diagram [41] for CGMs from the Li pegmatites at Kalu'an. The Ta and Mn enrichment trends for CGMs in fluorine-rich and fluorine-poor pegmatites are also based on [41]. Pegmatites of beryl and spodumene types are commonly F-poor whereas pegmatites of complex types are F-rich.

The core and rim of the CGMs in No. 803 pegmatite show consistent #Ta values (roughly 18.2 on average). The middle of the CGMs from this pegmatite consists of Nb-rich and Ta-rich domains based on #Ta values (Table 2). The Nb-rich domain has  $17.8 \pm 4.9$  #Ta whereas the Ta-rich domain  $48.6 \pm 9.9$  #Ta.

In No. 805 pegmatite, the #Ta value of CGM-I increases from  $14.9 \pm 3.3$  to  $79.8 \pm 7.1$  from the core to rim, whereas the #Mn value varies in a narrow range, indicating that the brightness variation of CGM-I on BSE images is mainly caused by Ta oscillation. During growth, the composition of CGM-I evolved towards tantalite-(Mn) (Figure 6), which suggests strong Nb-Ta fractionation. The #Mn and #Ta values of CGM-II are  $87.9 \pm 3.5$  and  $17.5 \pm 5.8$ . In summary, the CGMs from different Li pegmatites generally show comparable #Mn and #Ta values except for the rim of CGM-I in No. 805 pegmatite.

### 5.3. LA-ICP-MS Dating

The majority of CGM grains that were selected for LA-ICP-MS dating displayed oscillatory zoning and/or sector zoning. Figure 5 shows some representative dated CGM grains. The CGM-II from No. 805 pegmatite was not dated due to its small size.

Twenty-nine spots on twenty-seven CGM grains from No.802 pegmatite were analyzed. The apparent  $^{206}\text{Pb}/^{238}\text{U}$  ages range from 206.7 to 215.7 Ma, and the majority of the  $^{206}\text{Pb}/^{238}\text{U}$  ages are around 210 Ma (Figure 7, Table 3). Sixteen data points with age concordance >95% plot on the U-Pb Concordia, yielding a concordant age of  $209.5 \pm 1.4$  Ma (MSWD = 2.0) (Figure 8a). The same data points also yield a weighted mean  $^{206}\text{Pb}/^{238}\text{U}$  age of  $209.9 \pm 1.1$  Ma (MSWD = 1.9). The rest data points with discordant ages are below the Concordia (Figure 8a) and are, therefore, excluded for Concordia age calculation.

Twenty-five CGM grains from No. 803 pegmatite were dated. The apparent  $^{206}\text{Pb}/^{238}\text{U}$  ages mostly vary between 191.0 and 202.5 Ma (Figure 7, Table 3). Nineteen out of twenty-nine data points show age concordance >95% and plot on the U-Pb Concordia, yielding an age of  $198.3 \pm 2.0$  Ma (MSWD = 2.4) (Figure 8b). Within analytical errors, the corresponding weighted mean  $^{206}\text{Pb}/^{238}\text{U}$  age of those nineteen data points ( $197.4 \pm 1.3$  Ma, MSWD = 4.9) is identical to the concordant age. Two data points with discordant ages are above the Concordia whereas the rest data points showing discordant ages are below the Concordia (Figure 8b).

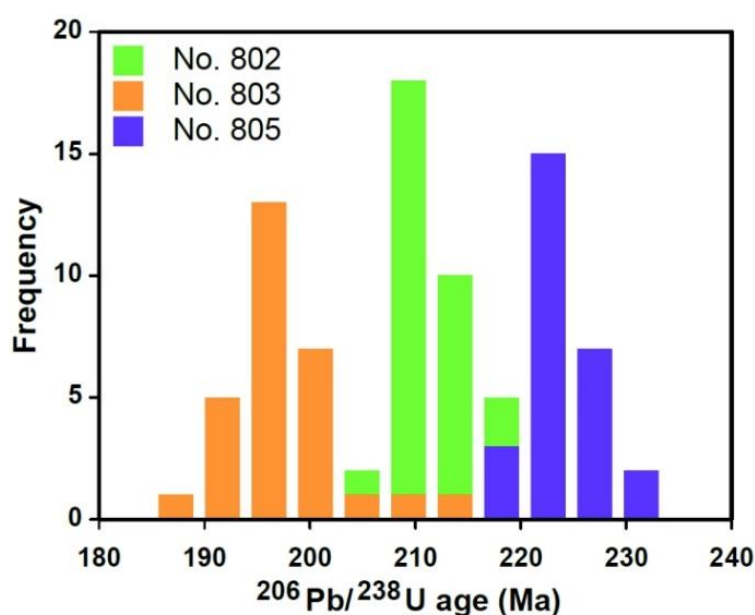
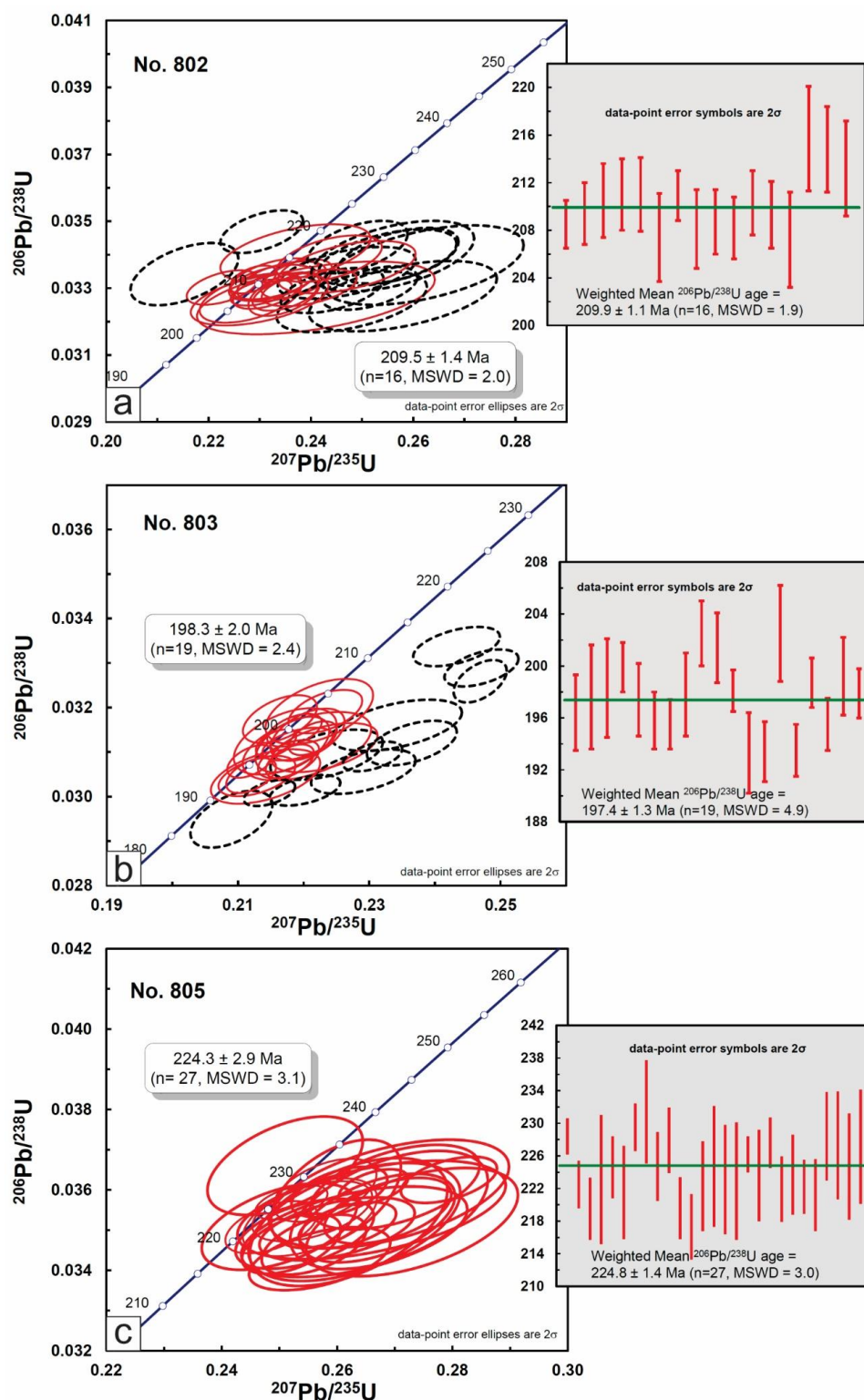


Figure 7. Histograms showing  $^{206}\text{Pb}/^{238}\text{U}$  age ranges for the studied pegmatites at Kalu'an.



**Figure 8.** U-Pb concordia diagram for CGMs from the Li-rich pegmatites at Kalu’an. (a) diagram showing a Concordia age of 209.5 ± 1.4 Ma for No. 802 pegmatite. (b) nineteen datapoints on the Concordia yielding 198.3 ± 2.0 Ma for No. 803 pegmatite. (c) diagram showing a Concordia age of 224.3 ± 2.9 Ma for No. 805 pegmatite.

Twenty-seven CGM grains from No. 805 pegmatite were dated. The apparent <sup>206</sup>Pb/<sup>238</sup>U ages mostly vary between 221.2 and 231.4 Ma (Figure 7, Table 3). All the data points plot on, or fairly close

to, the U-Pb Concordia (Figure 8c), yielding a concordant age of  $224.3 \pm 2.9$  Ma (MSWD = 3.1) and a weighted mean  $^{206}\text{Pb}/^{238}\text{U}$  age of  $224.8 \pm 1.4$  Ma (MSWD = 3.0).

The reasons for the variation in age data at pegmatite scale and the discordant ages are discussed in Section 6.1. The age data screening for Concordia age calculation is also justified in Section 6.1.

#### 5.4. LA-ICP-MS Trace Element Analysis

For all the studied pegmatites, the dated CGM grains with suitable grain sizes were selected for LA-ICP-MS trace element analysis. In addition, the rim of CGM-I and CGM-II from No. 805 pegmatite were analyzed.

For No. 802 pegmatite, 24 spots on the core of the CGM grains were analyzed. The Ca and REE concentrations are generally below the detection limits, except one analysis showing 64 ppm Ca (Table 4). The core of the CGMs from this pegmatite contains <1 ppm Sc, <1 ppm Y,  $328.9 \pm 143.8$  ppm Zr,  $10.1 \pm 3.7$  ppm Sn,  $25.4 \pm 10.8$  ppm Hf, and  $3581.1 \pm 983.0$  ppm W. The U, Th, and Pb concentrations are  $406.9 \pm 109.3$  ppm,  $12.3 \pm 6.8$  ppm, and  $73.6 \pm 37.1$  ppm, respectively.

The trace element concentrations of the CGMs from No. 803 pegmatite are generally consistent from the core to the rim (Table 4), although only one spot on the middle part of one CGM grain was analyzed due to the laser beam size. The Sc, Y, and REE concentrations are all below 1 ppm. The core contains  $9.6 \pm 4.1$  ppm Sn,  $517.5 \pm 220.0$  ppm Zr,  $38.3 \pm 9.2$  ppm Hf, and  $5468 \pm 1404$  ppm W, whereas the rim contains  $11.3 \pm 6.4$  ppm Sn and  $568.5 \pm 139.3$  ppm Zr,  $52.7 \pm 9.3$  ppm Hf, and  $5030.5 \pm 255.3$  W ppm. The U, Th, and Pb concentrations of the core are  $722.6 \pm 664.0$  ppm,  $29 \pm 37$  ppm, and  $132 \pm 130$  ppm, respectively, similar to those of the rim. It is noted that one analysis shows  $\sim 2000$  ppm U,  $>75$  ppm Th, and  $>300$  ppm Pb (Figure 9), which are obviously higher than the U, Th, and Pb concentrations of the other analyses. This may indicate the presence of U-rich inclusions on the analytical spot.

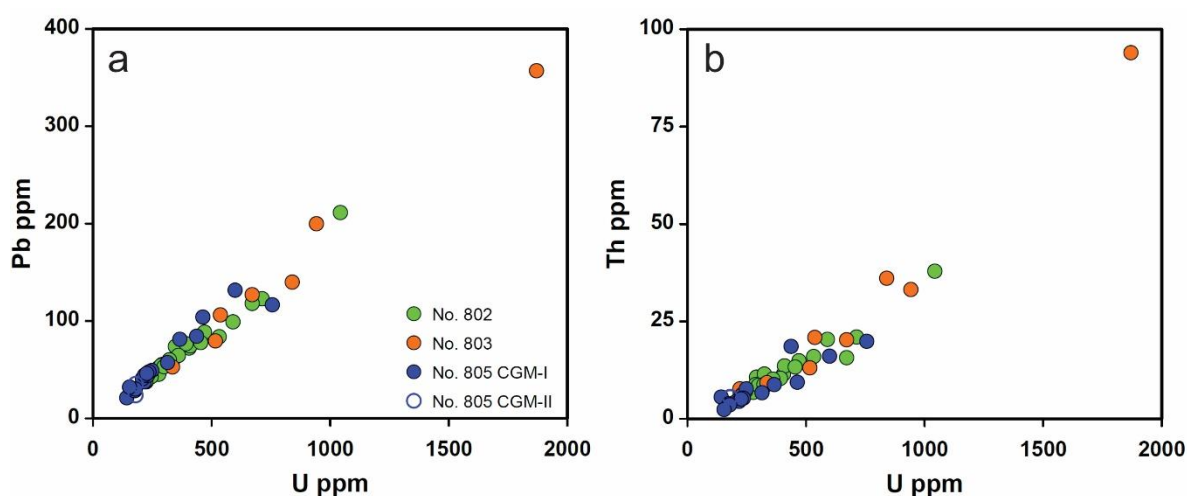


**Figure 9.** Binary plots for CGMs from the Li-rich pegmatites at Kalu'an. (a) Pb versus U plot and (b) Th versus U plot.

In No. 805 pegmatite, CGM-I contains <1 ppm Sc, <2 ppm Y, and  $\sim 3\text{--}7$  ppm Sn. The Zr, Hf, U, Th, and Pb concentrations are consistent from the core to the rim, with their mean values around 300–350 ppm, 30–50 ppm, 250–300 ppm, 5–10 ppm, and 50–60 ppm, respectively (Table 4). However, the W concentrations of CGM-I show variation from the core to the rim. The core contains  $4080.0 \pm 1273.9$  ppm W concentration, higher than the W concentrations (mostly <3000 ppm) of the middle and rim. The LREE concentrations are all below detection limits and the HREE concentrations are generally lower than 1 ppm. Only two spots on CGM-II were analyzed due to the small size. Compared to CGM-I, CGM-II contains relatively low Zr, Hf, U, Th, and Pb concentrations. The W concentration of CGM-II is lower than the core of CGM-I, but is similar to those of the middle and rim of CGM-I.

**Table 4.** Summary of trace element concentrations (in ppm) of CGMs obtained by LA-ICP-MS.

Pegmatite Comment	No. 802		No. 803					No. 805							
	Core		Core		Middle	Rim		CGM-I, core		CGM-I, middle		CGM-I, rim		CGM-II	
	mean (n = 24)	sd	mean (n = 5)	sd	n = 1	mean (n = 2)	sd	mean (n = 3)	sd	mean (n = 10)	sd	mean (n = 4)	sd	mean (n = 2)	sd
Ca	64 (1)	n.a.	72 (1)	n.a.	84.0	80 (1)	n.a.	b.d.	n.a.	77 (1)	n.a.	b.d.	n.a.	89 (1)	n.a.
Sc	0.26 (11)	0.07	0.42 (3)	0.16	0.55	0.4 (1)	n.a.	0.26 (1)	n.a.	0.37 (6)	0.11	0.27	0.09	0.35 (1)	n.a.
Y	0.17	0.07	0.42	0.41	0.09	0.36	0.23	0.72	0.90	1.44	0.63	0.45	0.18	0.49	0.01
Zr	328.9	143.8	517.5	220.0	572.0	568.5	139.3	348.1	100.8	347.5	156.7	281.6	158.4	107.0	24.3
Sn	10.1	3.7	9.6	4.1	10.5	11.3	6.4	5.4	2.8	3.7	0.8	4.21	1.40	6.14	0.98
La	b.d.	n.a.	0.03 (1)	n.a.	b.d.	b.d.	n.a.	b.d.	n.a.	b.d.	n.a.	b.d.	n.a.	b.d.	n.a.
Ce	b.d.	n.a.	0.19 (1)	n.a.	b.d.	b.d.	n.a.	b.d.	n.a.	0.06 (1)	n.a.	b.d.	n.a.	b.d.	n.a.
Dy	b.d.	n.a.	b.d.	n.a.	b.d.	b.d.	n.a.	0.21	n.a.	0.14 (5)	0.08	b.d.	n.a.	b.d.	n.a.
Ho	b.d.	n.a.	b.d.	n.a.	b.d.	b.d.	n.a.	0.06	n.a.	0.03 (9)	0.02	b.d.	n.a.	b.d.	n.a.
Er	b.d.	n.a.	0.10 (1)	n.a.	b.d.	b.d.	n.a.	0.15 (1)	n.a.	0.17	0.12	0.07	0.02	b.d.	n.a.
Tm	b.d.	n.a.	0.03 (1)	n.a.	b.d.	b.d.	n.a.	0.03 (2)	0.02	b.d.	0.06	0.03	0.02	0.01	0.04
Yb	0.13 (3)	0.02	0.16 (4)	0.13	b.d.	b.d.	n.a.	0.44	0.56	1.04	0.41	0.53	0.15	0.50	0.18
Lu	0.02 (2)	0	0.09 (1)	n.a.	b.d.	b.d.	n.a.	0.19 (1)	n.a.	0.2	0.1	0.09	0.02	0.09	0.03
Hf	25.4	10.8	38.3	9.2	52.5	52.7	9.3	33.7	13.1	51.5	28.2	49.4	26.3	9.4	5.6
W	3581.1	983.0	5468	1404	5260	5030.5	255.3	4080.0	1273.9	2611.0	419.6	2088.0	364.0	2712.0	463.9
Pb	73.6	37.1	132	130	140	153.1	66.2	57.1	24.4	61.4	37.0	53.2	34.7	29.6	8.2
Th	12.3	6.8	29	37	36	27.0	8.7	10.3	7.3	8.2	5.4	5.1	3.1	5.5	0.1
U	406.9	190.3	722.6	664.0	840.0	739.5	286.4	300.2	119.3	324.4	200.2	255.4	141.7	179.5	0.7

Note: The concentrations of Pr, Nd, Sm, Eu, Gd, and Tb of all the analyzed CGMs are below detection limits. “n” represents the number of analysis; numbers in the parentheses after the mean values of element concentrations indicate the number of analysis returning concentrations above the detection limits. Abbreviations: “b.d.” = below detection limit; “n.a.” = not available; “sd” = standard deviation.

Overall, the U and Pb concentrations of the dated CGMs show an excellent positive correlation (Figure 9a). The U and Th concentrations also exhibit positive correlation, except for one analysis on the CGMs from No. 803 pegmatite which shows extraordinarily high U and Th concentrations (Figure 9b).

Additionally, compared to the CGMs from No. 802 and No. 803 pegmatites, CGM-I from No. 805 pegmatite is generally characterized by relatively low W and Sn concentrations and low Zr/Hf ratio but relatively high and variable Y concentrations (Figure 10).

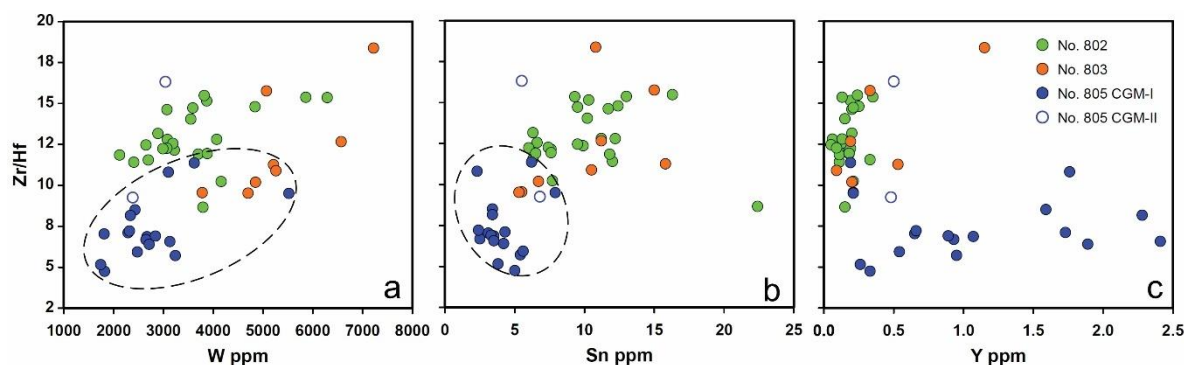


**Figure 10.** Correlations between Zr/Hf ratios and W, Sn, and Y concentrations of the CGMs from the Li-rich pegmatites at Kalu'an. (a) Zr/Hf ratio versus W, (b) Zr/Hf ratio versus Sn, and (c) Zr/Hf ratio versus Y.

## 6. Discussion

### 6.1. Age Variation at Pegmatite Scale

It is noted that  $^{206}\text{Pb}/^{238}\text{U}$  ages show variation at pegmatite scale (Figure 7). Also, the  $^{207}\text{Pb}/^{235}\text{U}$  ages show relatively large variation compared to the  $^{206}\text{Pb}/^{238}\text{U}$  ages, which was also observed by Che et al. [14]. Scrutiny of the columbite U-Pb age data for individual pegmatites indicates that the large age variation is mainly related to the discordant ages (Figure 8). For example, for No. 802 pegmatites, the data points with discordant ages show  $^{206}\text{Pb}/^{238}\text{U}$  ages ranging from  $219.8 \pm 3.2$  Ma to  $206.7 \pm 4.6$  Ma, whereas the data points with concordant ages show  $^{206}\text{Pb}/^{238}\text{U}$  ages varying within a smaller range ( $215.7 \pm 4.4$  Ma to  $207.2 \pm 4.0$  Ma) (Figure 8a, Table 3). For No. 803 pegmatites, the data points with discordant ages exhibit  $^{206}\text{Pb}/^{238}\text{U}$  ages ranging from  $211.6 \pm 2.3$  Ma to  $191.0 \pm 1.5$  Ma, whereas the data points with concordant ages show  $^{206}\text{Pb}/^{238}\text{U}$  ages varying between  $202.5 \pm 2.5$  Ma and  $187.3 \pm 3.2$  Ma.

Matrix effect during in situ dating may be another reason for the variation of the age data. Significant matrix effect during dating CGMs using SIMS was observed by [42]. According to [42], the matrix effect is mainly caused by #Ta values of CGMs, whereas #Mn values have no impact. However, the matrix effect during LA-ICP-MS U-Pb isotopic analyses were not encountered in most previous studies [14,21]. Only Smith et al. [13] suggested that the matrix effect potentially existed during dating of CGMs by LA-MC (multiple collector)-ICP-MS and could affect the accuracy of dating results. Che et al. [14] showed that dating of CGMs with compositions from ferrocolumbite to manganotantalite using a ferrocolumbite crystal (Coltan139) as the external standard did not result in noticeable matrix effect. In this study, we adopted the same analytical procedure and used the same external standard as in Che et al. [14]. Neither #Mn values nor #Ta values exhibit a correlation with  $^{206}\text{Pb}/^{238}\text{U}$  ages or  $^{207}\text{Pb}/^{235}\text{U}$  ages (Figure 11). For example, although the CGMs from No. 805 pegmatite show a large range of #Ta values, both the  $^{206}\text{Pb}/^{238}\text{U}$  ages and  $^{207}\text{Pb}/^{235}\text{U}$  ages are consistent (Figure 11c,d). According to LA-ICP-MS analysis, the CGMs from the Kalu'an lithium pegmatites contain significant W (2000–7000 ppm, Figure 10a). However, no matrix effect as a function of W concentration can be observed, either (Figure 12).

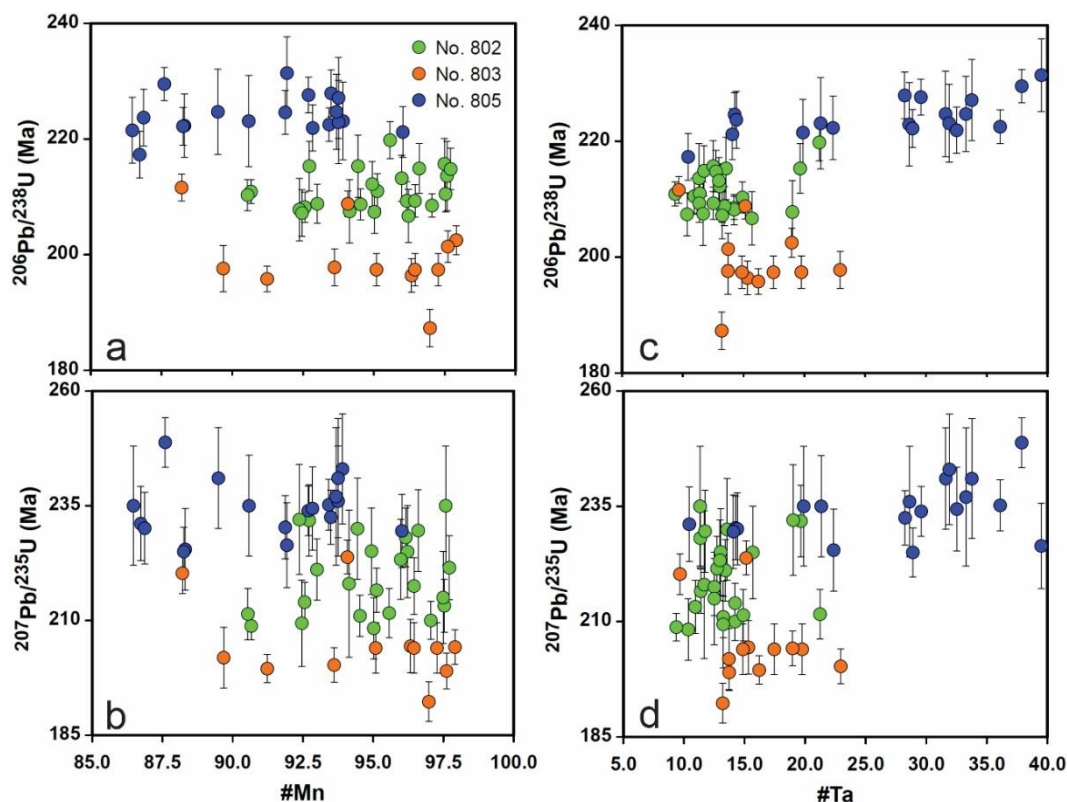


**Figure 11.** Binary plots showing correlations between columbite LA-ICP-MS U-Pb ages and #Mn and #Ta values of CGMs from the Kalu'an lithium pegmatites, (a) and (b) variations in  $^{206}\text{Pb}/^{238}\text{U}$  and  $^{207}\text{Pb}/^{235}\text{U}$  ages versus #Mn, (c) and (d) variations in  $^{206}\text{Pb}/^{238}\text{U}$  and  $^{207}\text{Pb}/^{235}\text{U}$  ages versus #Ta. The #Mn and #Ta values for the analytical spots on CGMs during LA-ICP-MS dating are based on the EPMA data for the same spots. The error bars represent the analytical errors ( $2\sigma$ ) for  $^{206}\text{Pb}/^{238}\text{U}$  and  $^{207}\text{Pb}/^{235}\text{U}$  ages. The dataset including U-Pb ages and the #Mn and #Ta values is provided in Supplementary Material Table S4.

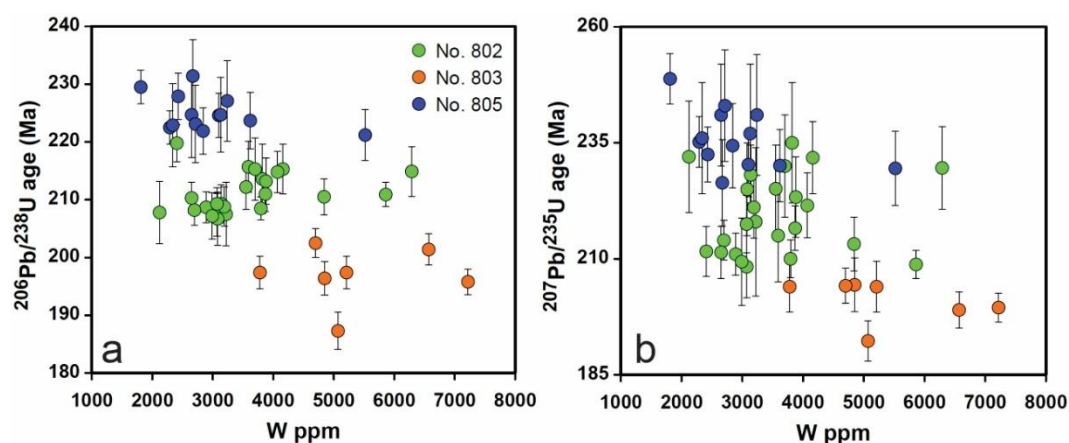


**Figure 12.** Binary plots showing correlations between columbite LA-ICP-MS U-Pb ages and the W concentrations of CGMs, (a) and (b) variations in  $^{206}\text{Pb}/^{238}\text{U}$  and  $^{207}\text{Pb}/^{235}\text{U}$  ages versus W. The error bars represent the analytical errors ( $2\sigma$ ) for  $^{206}\text{Pb}/^{238}\text{U}$  and  $^{207}\text{Pb}/^{235}\text{U}$  ages.

The discordant ages are likely caused by: (1) metamictization [43], (2) presence of U-rich inclusions [43], (3) common lead [42], and (4) microfractures. According to [43], both metamictization and presence of U-rich mineral inclusions (e.g., uraninite) can result in anomalous ages. The data points of the CGMs affected by these two factors would plot off the Concordia. As most analytical spots were examined using BSE imaging and U-rich mineral inclusions were avoided for most analyses,

presence of U-rich inclusions is not an important reason for the discordant ages. Some data points below the Concordia suggest potential Pb loss, which could be caused by metamictization. In this study, most dating analyses show high  $^{206}\text{Pb}/^{204}\text{Pb}$  ratios (mostly >1000) and the low Pb concentrations (mostly <150 ppm) (Figure 9a), indicating that the common Pb concentrations are mostly below the detection limit. Therefore, although the influence of common Pb may still exist, such influence is likely insignificant. In addition, secondary electron imaging shows that some of the discordant ages are likely caused by the presence of microfractures in the analyzed CGMs (see Figure 13 for example). In Figure 13, data points K805.6 and K805.15 are affected by microfractures and show age concordance <95%, although these two data points still plot close to the Concordia. Micro-scale inclusions (e.g., feldspar) may be present in the fractures [42] and would potentially affect the dating results. It is also noted that those microfractures were not obvious on BSE images but can be revealed using high-resolution SE imaging (Figure 13). Therefore, we excluded the dating analyses that were obviously affected by the presence of microfractures or possible metamictization for Concordia age calculation.

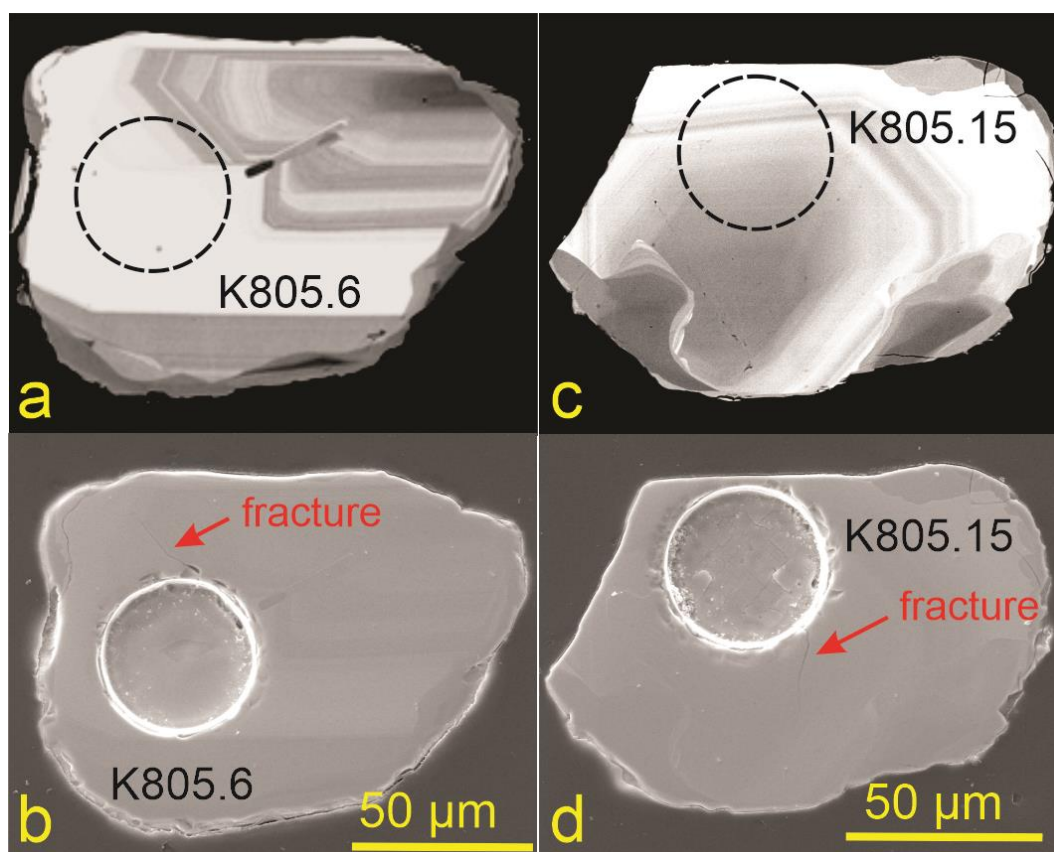


**Figure 13.** Backscattered electron (BSE) and secondary electron (SE) images showing that the discordant ages of some analytical spots are likely caused by the presence of fractures. (a) and (b) BSE and SE images of CGM K805.6. (c) and (d) BSE and SE images of CGM K805.15.

## 6.2. Emplacement Ages of the Kalu'an Li Pegmatites

The dated CGM grains exhibit oscillatory zoning and/or sector zoning (e.g., Figure 5), similar to typical magmatic CGMs in many granitic pegmatites [25,40,44–46]. Petrographic observations also reveal that columbite is associated with the primary mineral assemblage spodumene + albite + quartz + muscovite in the Li pegmatites (Figure 4). London [47] suggested that pegmatite-forming liquid likely starts crystallization at ~650 °C. In addition, granitic melts can be saturated with respect to columbite

at ~600–645 °C [47,48]. Therefore, the columbite U-Pb ages obtained in this study can represent the emplacement ages of the investigated Li pegmatites at Kalu'an.

The emplacement ages of No. 802, No. 803, and No. 805 pegmatites are  $209.5 \pm 1.4$  Ma ( $2\sigma$ ),  $198.3 \pm 2.0$  Ma ( $2\sigma$ ), and  $224.3 \pm 2.9$  Ma ( $2\sigma$ ), respectively. Previous studies reported zircon U-Pb ages for No. 803, No. 805, No. 806, No. 807, and No. 650 pegmatites at Kalu'an (Table 1). For No. 803 pegmatite, the zircon U-Pb age reported by [4] is over 20 Ma older than the columbite U-Pb age. For No. 805 pegmatite, the zircon U-Pb age reported by [3] is ~10 Ma younger than the columbite U-Pb age. The discrepancies are likely caused by the following factors. Firstly, the zircons dated in [3,4] were high-U zircons and lacked typical zonings of magmatic zircons in granitic rocks. According to their studies, the majority of zircons from No. 803 pegmatite contained 1913–70,047 ppm U whereas most zircons from No. 805 pegmatite contained 3400–16,457 ppm U. High U zircons frequently occur in highly evolved granites and pegmatites [21]. Such high U concentrations likely result in metamictization of zircons from those pegmatites and Pb loss (cf. [49]), which explains the discordant U-Pb ages in [3,4]. Secondly, although the high U effect during LA-ICP-MS dating of zircon is not as significant as that encountered during SHRIMP U-Pb dating of zircon, pulse-analog cross calibration must be performed to guarantee reliable U-Pb ages [50]. However, this calibration method was not mentioned in [3,4]. Finally, some of the high U zircons in their studies may have formed during late-stage alteration and yielded younger ages. Therefore, the reliability of the age data provided in [3,4] is questionable. By contrast, the columbite U-Pb ages for the studied Li pegmatites obtained in this study are concordant and are therefore more reliable.

The Li pegmatites can be broadly divided into two groups based on their strikes. The first group includes No. 802, No. 805, No. 806, and No. 650 pegmatite dikes that are nearly NS-striking (Figure 2). The emplacement ages of the first pegmatite group span from  $227.9 \pm 2.6$  Ma to  $209.5 \pm 1.4$  Ma. The emplacement age ( $224.3 \pm 2.9$  Ma) of No. 805 pegmatite is comparable to that ( $227.9 \pm 2.6$  Ma) of Stage 1 dike of No. 650 pegmatite (Table 1, Figure 2). In addition, the emplacement age ( $209.5 \pm 1.4$  Ma) of No. 802 pegmatite is similar to that ( $211.3 \pm 2.4$  Ma) of Stage 2 dike of No. 650 pegmatite (Table 1, Figure 2). Therefore, the first group of pegmatites formed at ~228–224 Ma and ~210 Ma. By contrast, the second group is mainly represented by No. 803 and No. 807 pegmatites that are NE to EW-striking. Although No. 807 pegmatite was dated by [3], only a lower-intercept age ( $221 \pm 15$  Ma) was reported. The large uncertainty indicates that this reported age is not accurate. The emplacement age of No. 803 pegmatite is ~10 Ma younger than the youngest pegmatite (No. 802 pegmatite) of the first group, suggesting that the second group of Li pegmatites likely formed later than the first group of Li pegmatites. In summary, in light of the latest age data, there were multiple emplacement events of Li pegmatite-forming melts in a timeframe of ~30 Ma at Kalu'an.

### 6.3. Implications for the Formation of the Kalu'an-Azubai Rare-Element Pegmatites

According to [4,5], the rare-element pegmatites in the Kalu'an-Azubai pegmatite field are typical LCT-family pegmatites, which exhibit geochemical signature similar to that of S-type granites derived from partial melting of (meta)sedimentary sources [51]. There are basically two schools of thought regarding the petrogenesis of rare-element pegmatites: (1) fractional crystallization of granitic magmas [37,47,51–53] and (2) direct anatexis [54–58]. The first model strongly relies on the granite-pegmatite relationship and the regional zonation of pegmatite groups that can reflect distinct differentiation of granitic magmas. For example, the Separation Rapids Pegmatite Group exhibits a clear genetic link to the nearby fertile S-type granitic pluton (the Separation Rapids pluton) [42]. However, this model often faces challenges in cases where no parental granites can be linked to rare-element pegmatites [57,59,60]. Alternatively, an anatectic origin has been proposed by several authors [55,57,58] to explain the formation of rare-element pegmatites without parental granitic plutons.

The rare-element pegmatites in the Kalu'an-Azubai region are at least 170 Ma younger than the nearby Halong granite ([3–5], this study). This indicates that the Halong granite cannot be the parental granite to the rare-element pegmatites. Additionally, to date, no granitic plutons with

ages similar to those of the rare-element pegmatites have been recognized in the Kalu'an-Azubai region and nearby areas [4]. Moreover, the timeframe of the Kalu'an-Azubai rare-element pegmatites reveals that the Li pegmatites were formed earlier than the Be-Ta-Nb pegmatites (~194–192 Ma [4,5]). This seemingly contradicts the typical fractionation course from barren pegmatites towards extremely Li-rich pegmatite proposed in previous studies [37]. Therefore, the newly established timeframe for the rare-metal pegmatites in the Kalu'an-Azubai region more likely favors an anatectic origin for the rare-metal pegmatites.

Zhang et al. [4] also proposed an anatectic origin for the rare-element pegmatites in this region in light of their obtained geochronological data and zircon Hf isotopes. According to their model, the pegmatite-forming melts were derived from a mixed source and the wide compositional spectrum of the pegmatites was likely due to different mixing ratios between two source components (the Halong granite and the Kulumuti group). However, using zircon Hf isotopic compositions to trace magma sources may be problematic because zircons may only record the Hf isotopic compositions of their surrounding melts, rather than directly represent the primary Hf isotopic compositions of the bulk magmas [61]. The study of Wang et al. [61] also shows that continental crust-derived melts would exhibit  $^{176}\text{Hf}/^{177}\text{Hf}$  ratios higher than their sources due to disequilibrium partial melting. Moreover, some zircons in the rare-element pegmatites in the Kalu'an-Azubai region could be xenocrystic or hydrothermal [4], and thus have no bearing on the Hf isotopic compositions of the pegmatite-forming melts. Therefore, the relatively high  $^{176}\text{Hf}/^{177}\text{Hf}$  ratios of zircons from the rare-element pegmatites in the Kalu'an-Azubai region may not reflect a mixture of the Halong granite and the Kulumuti group at the magma source.

## 7. Conclusions

This study demonstrates that the columbite-group minerals from the Kalu'an Li pegmatites have maintained primary internal textures, and that the U-Pb isotopic systematics of the CGMs has not been obviously affected by late-stage hydrothermal activities that affected the U-Pb ages of zircons from the same pegmatites. Moreover, no inherited columbite has been encountered. Matrix effect as a function of the compositions of CGMs was not observed during LA-ICP-MS dating. Therefore, columbite U-Pb dating can potentially provide unambiguous and precise concordant ages for the highly evolved Kalu'an Li pegmatites. Columbite U-Pb dating reveals that No. 802, 803, and 805 pegmatites at Kalu'an were emplaced at  $209.5 \pm 1.4$  Ma ( $2\sigma$ ),  $198.3 \pm 2.0$  Ma ( $2\sigma$ ), and  $224.3 \pm 2.9$  Ma ( $2\sigma$ ), respectively. The results indicate three emplacement events of Li pegmatite-forming melts in a timeframe of ~30 Ma at Kalu'an. In combination with previous studies on the same pegmatite field, the reconstructed timeframe for the Kalu'an-Azubai rare-element pegmatites show that the Li pegmatites were formed earlier than the Be-Ta-Nb pegmatites. This further supports an anatectic origin for the Kalu'an-Azubai rare-element pegmatites.

**Supplementary Materials:** The following are available online at <http://www.mdpi.com/2075-163X/9/8/456/s1>, Figure S1: BSE images showing laser ablation pits on the dated CGM grains, Table S1: Summarization on the standardization for EPMA analysis, Table S2: Complete dataset of EPMA analysis, Table S3: Complete dataset of LA-ICP-MS trace element analysis, Table S4: #Mn and #Ta values of the analytical spots for LA-ICP-MS dating.

**Author Contributions:** Y.F. conceived of the presented idea, designed the experiments and verified the data along with T.L. The article is originally written and revised by the corresponding author, Y.F., T.L., the other corresponding author is also responsible for key revisions. The financial support for this study was mainly secured by T.L., Y.F., H.W., Z.Z., Y.W., Y.Z., J.G., X.Y., and K.D. along with the two corresponding authors conducted the fieldwork. Z.Z. digitalized the geological map and performed EPMA analysis and LA-ICP-MS dating along with Y.F.

**Funding:** This study is financially supported by the Ministry of Science and Technology of the China granted to T. Liang (Grant Number: 2017YFC0602701) and the Fundamental Research Funds for the Central Universities of China to Y. Feng (Grant Number: 300102279101) and to H. Wang (Grant Number: 300102279401).

**Acknowledgments:** The authors are grateful to Huan Hu and Ennong Tian for the assistance with LA-ICP-MS dating. The authors would like to thank Zhongli Zhang and Zizhong Chen at Xinjiang Non-ferrous Metals Geological Exploration Bureau for fieldwork assistance. We are thankful to Marieke Van Lichtervelde and the

other four anonymous reviewers and the academic editor for their comments that helped improve this manuscript significantly. Y. Feng is grateful to the China Scholarship Council for financial support.

**Conflicts of Interest:** The authors declare no conflict of interest.

## References

1. Wang, D.H.; Chen, Y.C.; Xu, Z.G. *Metallogenic Series and Regularity of the Altay Metallogenic Province*; Atomic Energy Press: Beijing, China, 2002; pp. 1–493. (In Chinese)
2. Zou, T.R.; Li, Q.C. *Rare and Rare Earth Metallic Deposits in Xinjiang, China*; Geological Publishing House: Beijing, China, 2006; p. 284. (In Chinese with English abstract).
3. Ma, Z.L.; Zhang, H.; Tang, Y.; Lv, Z.H.; Zhang, X.; Zhao, J.Y. Zircon U-Pb geochronology and Hf isotopes of pegmatites from the Kaluan mining area in the Altay, Xinjiang and their genetic relationship with the Halong granite. *Geochimica* **2015**, *44*, 9–26.
4. Zhang, X.; Zhang, H.; Ma, Z.L.; Tang, Y.; Lv, Z.H.; Zhao, J.Y.; Liu, Y.L. A new model for the granite-pegmatite genetic relationships in the Kaluan–Azubai–Qiongkuer pegmatite-related ore fields, the Chinese Altay. *J. Asian Earth Sci.* **2016**, *124*, 139–155. [[CrossRef](#)]
5. Zhou, Q.; Qin, K.; Tang, D.; Wang, C.; Sakyi, P. LA-ICP-MS U-Pb zircon, columbite-tantalite and  $^{40}\text{Ar}$ - $^{39}\text{Ar}$  muscovite age constraints for the rare-element pegmatite dykes in the Altai orogenic belt, NW China. *Geol. Mag.* **2018**, *155*, 707–728. [[CrossRef](#)]
6. Linnen, R.L.; Van Lichtenvelde, M.; Černý, P. Granitic pegmatites as sources of strategic metals. *Elements* **2012**, *8*, 275–280. [[CrossRef](#)]
7. Linnen, R.L.; Samson, I.M.; Williams-Jones, A.E.; Chakhmouradian, A.R. Geochemistry of the rare-earth element, Nb, Ta, Hf, and Zr deposits. In *Treatise on Geochemistry*, 2nd ed.; Holland, H.D., Turekian, K.K., Eds.; Elsevier: Oxford, UK, 2014; Volume 13, pp. 543–564.
8. Černý, P.; Ercit, T.S. Mineralogy of niobium and tantalum: Crystal chemical relationships, paragenetic aspects and their economic implications. In *Lanthanides. Tantalum and Niobium*; Möller, P., Černý, P., Saupé, F., Eds.; Springer: Berlin, Germany, 1989; pp. 27–79.
9. Ercit, T.S. The geochemistry and crystal chemistry of columbite-group minerals from granitic pegmatites, southwestern Grenville province, Canadian Shield. *Can. Mineral.* **1994**, *32*, 421–438.
10. Romer, R.L.; Smeds, S.A.; Černý, P. Crystal-chemical and genetic controls of U-Pb systematics of columbite-tantalite. *Mineral. Petrol.* **1996**, *57*, 243–260. [[CrossRef](#)]
11. Melcher, F.; Graupner, T.; Gäbler, H.-E.; Sitnikova, M.; Henjes-Kunst, F.; Oberthür, T.; Gerdes, A.; Dewaele, S. Tantalum-(niobium-tin) mineralisation in African pegmatites and rare metal granites: Constraints from Ta-Nb oxide mineralogy, geochemistry and U-Pb geochronology. *Ore Geol. Rev.* **2015**, *64*, 667–719. [[CrossRef](#)]
12. Romer, R.L.; Wright, J.E. U-Pb dating of columbites: A geochronologic tool to date magmatism and ore deposits. *Geochim. Cosmochim. Acta* **1992**, *56*, 2137–2142. [[CrossRef](#)]
13. Smith, S.R.; Foster, G.L.; Romer, R.L.; Tindle, A.G.; Kelley, S.P.; Noble, S.R.; Horsthood, M.; Breaks, F.W. U-Pb columbite-tantalite chronology of rare-element pegmatites using TIMS and laser ablation multi collector-ICP-MS. *Contrib. Mineral. and Petrol.* **2004**, *147*, 549–564. [[CrossRef](#)]
14. Che, X.D.; Wu, F.Y.; Wang, R.C.; Gerdes, A.; Ji, W.Q.; Zhao, Z.H.; Yang, J.H.; Zhu, Z.Y. In situ U-Pb isotopic dating of columbite-tantalite by LA-ICPMS. *Ore Geol. Rev.* **2015**, *65*, 979–989. [[CrossRef](#)]
15. Romer, R.L.; Lehmann, B. U-Pb columbite age of Neoproterozoic Ta-Nb mineralization in Burundi. *Econ. Geol.* **1995**, *90*, 2303–2309. [[CrossRef](#)]
16. Romer, R.L.; Smeds, S.A. U-Pb columbite chronology of post-kinematic Palaeoproterozoic pegmatites in Sweden. *Precambrian Res.* **1997**, *82*, 85–99. [[CrossRef](#)]
17. Romer, R.L.; Smeds, S.A. U-Pb columbite ages of pegmatites from Sveconorwegian terranes in southwestern Sweden. *Precambrian Res.* **1996**, *76*, 15–30. [[CrossRef](#)]
18. Romer, R.L.; Smeds, S.A. Implications of U-Pb ages of columbite-tantalites from granitic pegmatites for the Palaeoproterozoic accretion of 1.90–1.85 Ga magmatic arcs to the Baltic Shield. *Precambrian Res.* **1994**, *67*, 141–158. [[CrossRef](#)]
19. Baumgartner, R.; Romer, R.L.; Moritz, R.; Sallet, R.; Chiaradia, M. Columbite-tantalite bearing granitic pegmatites from the Seridó Belt, northeastern Brazil: Genetic constraints from U-Pb dating and Pb isotopes. *Can. Mineral.* **2006**, *44*, 69–86. [[CrossRef](#)]

20. Melleton, J.; Gloaguen, E.; Frei, D.; Novák, M.; Breiter, K. How are the emplacement of rare-element pegmatites, regional metamorphism and magmatism interrelated in the Moldanubian Domain of the Variscan Bohemian Massif, Czech Republic? *Can. Mineral.* **2012**, *50*, 1751–1773. [[CrossRef](#)]
21. Deng, X.D.; Li, J.W.; Zhao, X.F.; Hu, Z.C.; Hu, H.; Selby, D.; Souza, Z.S.D. U-Pb isotope and trace element analysis of columbite-(Mn) and zircon by laser ablation ICP-MS: implications for geochronology of pegmatite and associated ore deposits. *Chem. Geol.* **2013**, *344*, 1–11. [[CrossRef](#)]
22. Che, X.D.; Wang, R.C.; Wu, F.Y.; Zhu, Z.Y.; Zhang, W.L.; Hu, H.; Xie, L.; Lu, J.J.; Zhang, D. Episodic Nb-Ta mineralisation in South China: Constraints from in situ LA-ICP-MS columbite-tantalite U-Pb dating. *Ore Geol. Rev.* **2019**, *105*, 71–85. [[CrossRef](#)]
23. Lupulescu, M.; Chiarenzelli, J.; Pecha, M.; Singer, J.; Regan, S. Columbite-group minerals from New York pegmatites: Insights from isotopic and geochemical analyses. *Geosciences* **2018**, *8*, 169. [[CrossRef](#)]
24. Fosso Tchunte, P.M.; Tchameni, R.; André-Mayer, A.S.; Dakoure, H.S.; Turlin, F.; Poujol, M.; Negue Nomo, E.; Saha Fouotsa, A.N.; Rouer, O. Evidence for Nb-Ta Occurrences in the Syn-Tectonic Pan-African Mayo Salah leucogranite (Northern Cameroon): Constraints from Nb-Ta oxide mineralogy, geochemistry and U-Pb LA-ICP-MS geochronology on columbite and monazite. *Minerals* **2018**, *8*, 188. [[CrossRef](#)]
25. Van Lichtervelde, M.; Salvi, S.; Beziat, D.; Linnen, R.L. Textural features and chemical evolution in tantalum oxides: Magmatic versus hydrothermal origins for Ta mineralization in the Tanco Lower pegmatite, Manitoba, Canada. *Econ. Geol.* **2007**, *102*, 257–276. [[CrossRef](#)]
26. Windley, B.F.; Kröner, A.; Guo, J.; Qu, G.; Li, Y.; Zhang, C. Neoproterozoic to Paleozoic geology of the Altai orogen, NW China: New zircon age data and tectonic evolution. *J. Geol.* **2002**, *110*, 719–737. [[CrossRef](#)]
27. Windley, B.F.; Alexeiev, D.; Xiao, W.J.; Kröner, A.; Badarch, G. Tectonic models for accretion of the Central Asian Orogenic Belt. *J. Geol. Soc.* **2007**, *164*, 31–47. [[CrossRef](#)]
28. Xiao, W.J.; Windley, B.F.; Badarch, G.; Sun, S.; Li, J.L.; Qin, K.Z.; Wang, Z. Palaeozoic accretionary and convergent tectonics of the southern Altai: Implications for the growth of central Asia. *J. Geol. Soc. Lond.* **2004**, *161*, 339–342. [[CrossRef](#)]
29. Long, X.P.; Yuan, C.; Sun, M.; Xiao, W.J.; Zhao, G.C.; Wang, Y.J.; Cai, K.D. Detrital zircon ages and Hf isotopes of the early Paleozoic Flysch sequence in the Chinese Altai, NW China: New constraints on depositional age, provenance and tectonic evolution. *Tectonophysics* **2010**, *180*, 213–231. [[CrossRef](#)]
30. Long, X.P.; Sun, M.; Yuan, C.; Xiao, W.J.; Cai, K.D. Early Paleozoic sedimentary record of the Chinese Altai: Implications for its tectonic evolution. *Sed. Geol.* **2008**, *208*, 88–100. [[CrossRef](#)]
31. Long, X.P.; Sun, M.; Yuan, C.; Xiao, W.J.; Lin, S.F.; Wu, F.Y.; Xia, X.P.; Cai, K.D. U-Pb and Hf isotopic study of zircons from metasedimentary rocks in the Chinese Altai: Implications for Early Palaeozoic tectonic evolution. *Tectonics* **2007**, *26*, TC5015. [[CrossRef](#)]
32. Sun, G.H.; Li, J.Y.; Yang, T.N.; Li, Y.P.; Zhu, Z.X.; Yang, Z.Q. Zircon SHRIMP U-Pb dating of two linear granite plutons in southern Altay Mountains and its tectonic implications. *Geol. China* **2009**, *36*, 976–987, (In Chinese with English abstract).
33. Sun, M.; Long, X.P.; Cai, K.D.; Jiang, Y.D.; Wong, P.W.; Yuan, C.; Zhao, G.C.; Xiao, W.J.; Wu, F.Y. Early Paleozoic ridge subduction in the Chinese Altai: Insight from the abrupt change in zircon Hf isotopic compositions. *Sci. China Ser. D: Earth Sci.* **2009**, *39*, 1–14. [[CrossRef](#)]
34. Pirajno, F.; Seltmann, R.; Yang, Y. A review of mineral systems and associated tectonic settings of northern Xinjiang, NW China. *Geosci. Front.* **2011**, *2*, 157–185. [[CrossRef](#)]
35. Qin, K.; Shen, M.; Tang, D.; Guo, Z.; Zhou, Q.; Wang, C.; Guo, X.; Tian, Y.; Ding, J. Types, intrusive and mineralization ages of pegmatite rare-element deposits in Chinese Altay. *Xinjiang Geol.* **2013**, *31*, 1–7, (In Chinese with English abstract).
36. Wang, Y.J.; Long, X.P.; Wilde, S.A.; Xu, H.L.; Sun, M.; Xiao, W.J.; Yuan, C.; Cai, K.D. Provenance of Early Paleozoic metasediments in the central Chinese Altai: Implications for tectonic affinity of the Altai-Mongolia terrane in the Central Asian Orogenic Belt. *Lithos* **2014**, *210*, 57–68. [[CrossRef](#)]
37. London, D. Pegmatites. In *The Canadian Mineralogist*; Special Publication: London, UK, 2008; p. 347.
38. Hellstrom, J.; Paton, C.; Woodhead, J.; Hergt, J. Iolite: Software for spatially resolved LA-(quad and MC) ICPMS analysis. *Mineral. Assoc. Can. short course Ser.* **2008**, *40*, 343–348.
39. Ludwig, K.R. User's manual for Isoplot/Ex, Version 3.00: A Geochronological Toolkit for Microsoft Excel. *Berkeley Geochronol. Cent. Spec. Publ.* **2003**, *4*, 1–70.

40. Feng, Y.; Liang, T.; Yang, X.; Zhang, Z.; Wang, Y. Chemical evolution of Nb-Ta oxides and cassiterite in phosphorus-rich albite-spodumene pegmatites in the Kangxiwa–Dahongliutan pegmatite field, Western Kunlun Orogen, China. *Minerals* **2019**, *9*, 166. [[CrossRef](#)]
41. Černý, P. Characteristics of pegmatite deposits of tantalum. In *Lanthanides, Tantalum and Niobium*; Möller, P., Černý, F., Saupé, F., Eds.; Springer: Berlin, Germany, 1989; pp. 195–239.
42. Legros, H.; Mercadier, J.; Villeneuve, J.; Romer, R.L.; Deloule, E.; Van Lichtenvelde, M.; Dewaele, S.; Lach, P.; Che, X.D.; Wang, R.C.; et al. U-Pb isotopic dating of columbite-tantalite minerals: Development of reference materials and in situ applications by ion microprobe. *Chem. Geol.* **2019**, *512*, 69–84. [[CrossRef](#)]
43. Romer, R.L. Alpha-recoil in U-Pb geochronology: effective sample size matters. *Contrib. Mineral. Petrol.* **2003**, *145*, 481–491. [[CrossRef](#)]
44. Černý, P.; Novák, M.; Chapman, R. Effects of sillimanite-grade metamorphism and shearing on Nb-Ta oxide minerals in granitic pegmatites: Marsikov, Northern Moravia, Czechoslovakia. *Can. Mineral.* **1992**, *30*, 699.
45. Tindle, A.G.; Breaks, F.W. Columbite-tantalite mineral chemistry from rare-element granitic pegmatites: Separation Lake area, N.W. Ontario, Canada. *Mineral. Petrol.* **2000**, *70*, 165–198. [[CrossRef](#)]
46. Badanina, E.V.; Sitnikova, M.A.; Gordienko, V.V.; Melcher, F.; Gäbler, H.E.; Lodziak, J.; Syritso, L.F. Mineral chemistry of columbite-tantalite from spodumene pegmatites of Kolmozero, Kola Peninsula (Russia). *Ore Geol. Rev.* **2015**, *64*, 720–735. [[CrossRef](#)]
47. London, D. Ore-forming processes within granitic pegmatites. *Ore Geol. Rev.* **2018**, *101*, 349–383. [[CrossRef](#)]
48. Linnen, R.L. Depth of emplacement, fluid provenance and metallogeny in granitic terranes: A comparison of western Thailand with other tin belts. *Miner. Depos.* **1998**, *33*, 461–476. [[CrossRef](#)]
49. White, L.T.; Ireland, T.R. High-uranium matrix effect in zircon and its implications for SHRIMP U-Pb age determinations. *Chem. Geol.* **2012**, *306*, 78–91. [[CrossRef](#)]
50. Zhao, K.D.; Jiang, S.Y.; Ling, H.F.; Palmer, M.R. Reliability of LA-ICP-MS U-Pb dating of zircons with high U concentrations: A case study from the U-bearing Douzhashan Granite in South China. *Chem. Geol.* **2014**, *389*, 110–121. [[CrossRef](#)]
51. Černý, P.; London, D.; Novák, M. Granitic pegmatites as reflections of their sources. *Elements* **2012**, *8*, 289–294. [[CrossRef](#)]
52. Černý, P. Rare-element granitic pegmatites. Part II: Regional to global environments and petrogenesis. *Geosci. Can.* **1991**, *18*, 2.
53. London, D.; Morgan, G.B. The pegmatite puzzle. *Elements* **2012**, *8*, 263–268. [[CrossRef](#)]
54. Shearer, C.K.; Papike, J.J.; Jolliff, B.L. Petrogenetic links among granites and pegmatites in the Harney Peak rare-element granite-pegmatite system, Black Hills, South Dakota. *Can. Mineral.* **1992**, *30*, 785–809.
55. Martin, R.F.; De Vito, C. The patterns of enrichment in felsic pegmatites ultimately depend on tectonic setting. *Can. Mineral.* **2005**, *43*, 2027–2048. [[CrossRef](#)]
56. Simmons, W.B.S.; Webber, K.L. Pegmatite genesis: State of the art. *Eur. J. Mineral.* **2008**, *20*, 421–438. [[CrossRef](#)]
57. Konzett, J.; Schneider, T.; Nedyalkova, L.; Hauzenberger, C.; Melcher, F.; Gerdes, A.; Whitehouse, M. Anatectic granitic pegmatites from the eastern Alps: A case of variable rare-metal enrichment during high-grade regional metamorphism—I: Mineral assemblages, geochemical characteristics, and emplacement ages. *Can. Mineral.* **2018**, *56*, 555–602. [[CrossRef](#)]
58. Konzett, J.; Hauzenberger, C.; Ludwig, T.; Stalder, R. Anatectic granitic pegmatites from the eastern Alps: A case of variable rare metal enrichment during high-grade regional metamorphism. II: Pegmatite staurolite as an indicator of anatectic pegmatite parent melt formation—A field and experimental study. *Can. Mineral.* **2018**, *56*, 603–624. [[CrossRef](#)]
59. Stewart, D.B. Petrogenesis of lithium-rich pegmatites. *Am. Mineral.* **1978**, *63*, 970–980.
60. Swanson, S.E. Mineralogy of spodumene pegmatites and related rocks in the tin-spodumene belt of North Carolina and South Carolina, USA. *Can. Mineral.* **2012**, *50*, 1589–1608. [[CrossRef](#)]
61. Wang, D.; Wang, X.L.; Cai, Y.; Goldstein, S.L.; Yang, T. Do Hf isotopes in magmatic zircons represent those of their host rocks? *J. Asian Earth Sci.* **2018**, *154*, 202–212. [[CrossRef](#)]

